

JGR Solid Earth

RESEARCH ARTICLE

10.1029/2021JB021717

Key Points:

- Ocean bottom seismometer records from the northwest Pacific reveal strong azimuthal variation in *Po/So* propagation characteristics
- Numerical simulation confirms the variations can be explained by laterally elongated fine-scale heterogeneity in the oceanic lithosphere
- The configuration of the heterogeneity helps to guide significant energy from deep in-slab earthquakes in the Pacific plate

Supporting Information:

Supporting Information may be found in the online version of this article.

Correspondence to:

T. Furumura,
furumura@eri.u-tokyo.ac.jp



Citation:

Furumura, T., & Kennett, B. L. N. (2021). Azimuthal variation of lithospheric heterogeneity in the Northwest Pacific inferred from *Po/So* propagation characteristics and anomalously large ground motion of deep in-slab earthquakes. *Journal of Geophysical Research: Solid Earth*, 126, e2021JB021717. <https://doi.org/10.1029/2021JB021717>

Received 15 JAN 2021
Accepted 3 MAY 2021

© 2021. American Geophysical Union.
All Rights Reserved.

Azimuthal Variation of Lithospheric Heterogeneity in the Northwest Pacific Inferred From *Po/So* Propagation Characteristics and Anomalously Large Ground Motion of Deep In-Slab Earthquakes

Takashi Furumura¹  and Brian L. N. Kennett² 

¹Earthquake Research Institute, The University of Tokyo, Bunkyo, Japan, ²Research School of Earth Sciences, The Australian National University, Canberra, ACT, Australia

Abstract High-frequency oceanic *Pn/Sn* (*Po/So*) phases (>2 Hz) recorded at ocean bottom seismometers in the northwest Pacific display strong azimuthal variations in propagation characteristics. In the direction parallel to former Pacific plate motion (N30°W), seismograms show a gentle rise at the onset of *Po/So* followed by large, long spindle-shaped coda; *Po* has a low-frequency (<0.25 Hz) precursor and much delayed high-frequency signals, showing weak dispersion with frequency. For orthogonal propagation, the onset of *Po/So* rises sharply and bursts of *Po* reverberations in the seawater follow. These differences indicate a strong azimuthal dependence of the scattering waveguide effect of the oceanic lithosphere. Numerical simulations of seismic waves in three-dimensional heterogeneous structures reveal that much of the observed *Po/So* propagation variability can be explained by laterally elongated fine-scale heterogeneity in the oceanic lithosphere, with a correlation distance of 20 km in the direction parallel to the magnetic anomaly, and a much shorter correlation distance in the perpendicular and depth directions. The longer axis corresponds to the observed *Pn/Sn*-wavespeed anisotropy in the northwest Pacific, so the heterogeneity pattern was also developed during the formation and growth of the Pacific plate; competing processes produce different styles of fine-scale effects. The elongated heterogeneity distributions in the oceanic lithosphere are carried into the subducting Pacific slab allowing energy from deep-focus earthquakes to propagate to large distances, producing observations of anomalously large ground motions in specific directions. The behavior can be matched with three-dimensional simulation of high-frequency wave propagation with a heterogeneous Pacific slab.

1. Introduction

Oceanic *Pn/Sn* waves, which are often referred to as *Po/So*, are characterized by high-frequency (>2 Hz) arrivals with a long coda that travel for more than 2,000 km across the Pacific (Walker & Sutton, 1971). Fine-scale heterogeneity in the oceanic lithosphere with much longer horizontal than vertical correlation length produces multiple forward scattering of high-frequency waves within the lamella that guide high-frequency signals for large distances. The scattering waveguide effect of the heterogeneous lithosphere is further reinforced by seawater trapped *P* waves that interacts with *Po* and *So* at the seafloor (Kennett & Furumura, 2013).

The propagation and attenuation properties of *Po/So* depends strongly on the thickness of the lithospheric waveguide. Propagation is efficient in the thick, old (120 Ma) northwest part of the Pacific Plate. However, attenuation is significant in propagation across the thin, younger (30 Ma) Philippine-Sea Plate (Kennett & Furumura, 2013; Shito et al., 2013). The *Po/So* propagation intensity has a positive relationship with the age of the Pacific plate, that is the thickness of oceanic lithosphere (Kennett et al., 2014) and is also the case with the Philippine-Sea plate (Shito et al., 2015).

Kennett and Furumura (2013) demonstrated that the general properties of oceanic *Po* and *So* traveling through the scattering waveguide can be captured by a stochastic heterogeneity model for the lithospheric mantle with much longer horizontal correlation distance ($a_h = 10$ km) than in the vertical direction ($a_z = 0.5$ km). A suitable description is provided by, for example, the von Kármán stochastic random heterogeneity model (e.g., see Frankel & Clayton, 1986) with 2% standard deviation of the root-mean-square

(r.m.s.) *P*- and *S*-wavespeed fluctuations from averaged background wavespeeds and 1.6% in density. The heterogeneity produces multiple forward scattering of high-frequency *Po* and *So* by interaction with fine-scale quasi-lamina structure (Kennett et al., 2014). These models use a uniform amplitude of heterogeneity through the lithosphere, and when linked with variations in background velocity structure provide a good representation of observation across the Pacific basin. However, a constant heterogeneity distribution throughout the lithosphere does not have an obvious geological origin. Kennett and Furumura (2015) have shown that a modified distribution with stronger heterogeneity at the base of the mantle lithosphere (2.5%), decreasing to 0.5% at the crust-mantle boundary provides a better representation of the character of *Po* and *So*, whilst linking directly to ideas about progressive accretion of material to the base of the oceanic plate as it cools (Hirschmann, 2010).

Such a fine-scale heterogeneous structure in the oceanic lithosphere guides high-frequency signals to great distances, and its extension into subduction zones plays a major role in shaping the geographic distribution of strong ground motion from deep earthquakes as demonstrated by 2-D numerical simulation of seismic wave propagation (Furumura & Kennett, 2005, 2008; Kennett & Furumura, 2008).

Previous studies of *Po/So* have been limited to investigating wave propagation in 2-D. However, the nature of 3-D propagation is important for understanding the origin of lithospheric heterogeneity, and for full simulations of expected strong ground motion from subduction zone earthquakes. Until recently the available paths have been insufficient to characterize the full azimuthal character of *Po/So* propagation, and computations have been restricted to 2-D structures for high frequencies.

Long-term observations from a broadband OBS network (Shiobara et al., 2005) in the northwest Pacific supplemented by the array experiments of the *NOMan* project operated by the Ocean Hemisphere Center at the Earthquake Research Institute, the University of Tokyo, coupled with the relatively high seismic activity in the northwest Pacific subduction zone before and after the great Off-Tohoku earthquake in 2011 mean it is now possible to examine the azimuthal variation of *Po/So* propagation characteristics across the northwest Pacific (Figure 1).

There are distinct differences in the character of the *Po/So* phases that depend on the location of the sources. *Po/So* from Kamchatka earthquakes, north of the OBS array, have a sharp rise in the onset of *Po/So*, while events off the east coast of Tohoku, Japan, southwest of the array, have a spindle-shaped onset for *Po/So* with long coda (Figure 2). These differences suggest azimuthal variations in the fine-scale heterogeneity distribution in the oceanic lithosphere. The directions for which a sharp *Po/So* rise is observed align with the orientation where maximum *Pn*-wavespeed anisotropy has been reported (e.g., Shimamura, 1984; Shinohara et al., 2008). This direction corresponds to the former motion of the Pacific Plate motion before 40 Ma, as inferred from the stripes of magnetic anomalies on the seafloor in the northwest Pacific (Meyer et al., 2017; Nakanishi et al., 1989). Thus, the heterogeneity distribution in the oceanic lithosphere is likely to be produced during the formation and spreading processes of the Pacific plate, that also result in the creation of *Pn*-wavespeed anisotropy.

In this study we conduct three-dimensional (3-D) finite-difference method (FDM) simulations of high-frequency wave propagation using a recently deployed high-performance supercomputer with a laterally heterogeneous oceanic lithosphere model to examine the observed *Po/So* wave propagation anomaly in the northwest Pacific. The results of the simulations show that a good representation of the observed azimuthal variation in *Po/So* propagation characteristics in the northwest Pacific is provided by laterally elongated fine-scale heterogeneity structure in the lithosphere with a longer correlation distance of 20 km in the direction N60°E, parallel to the magnetic anomaly pattern, and much shorter correlation distances in the orthogonal (1 and 5 km) and vertical (0.5 km) directions. Processes in the growth and spread of the plate impose complex fine-scale structure with competition between near-surface and basal effects with different correlation lengths. Such laterally elongated heterogeneity in the oceanic lithosphere can guide high-frequency *Po/So* very efficiently in the direction parallel to the long axis of the heterogeneity distribution and develop strong azimuthal variation of propagation characteristics.

The subducted oceanic lithosphere carries its laterally elongated fine-scale heterogeneity into the Pacific slab beneath Japan. The configuration of the heterogeneity helps to guide significant energy from deep in-slab earthquakes with enhancement along the direction of longest correlation. Such an enhanced waveguide

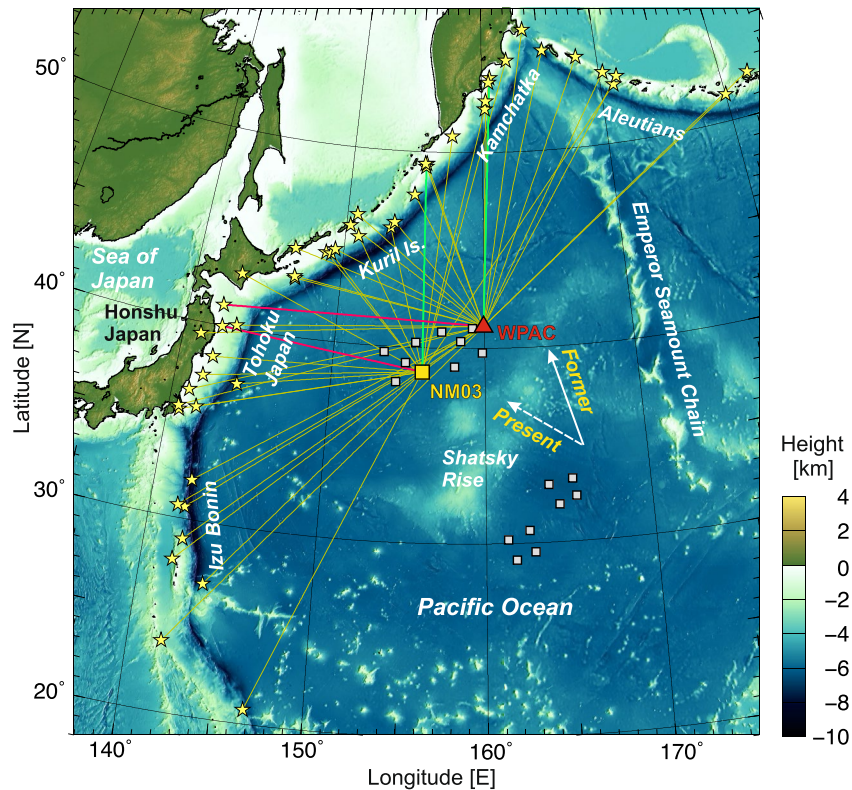


Figure 1. Map showing the location of the northern OBS array of the *NOMan* project of the Ocean Hemisphere Research Center at Earthquake Research Institute, the University of Tokyo shown by gray boxes. The stations WPAC and NM03 used in this study are identified together with the paths analyzed for the *Po/So* phases from the earthquakes in the surrounding subduction zones: from the Aleutians, Kamchatka, Kuril, Japan, to the Izu-Bonin arc. Bathymetric data were obtained from SRTM15+ Global bathymetry and topography data (Tozer et al., 2019). Arrows show directions of the former (before 40 Ma) and present Pacific Plate motions relative to Eurasia plate, calculated using the NUVEL-1A model (DeMets et al., 1994) at the location of WPAC (41.1°N, 159.9°E).

effect for deep in-slab earthquakes in the Pacific plate is demonstrated by 3-D simulation of high-frequency wave propagation for the July 16, 2007, Mw 6.8 earthquake beneath the Sea of Japan at a depth of 384 km, which showed anomalously large shaking 1,000 km away from the epicenter.

2. *Po* and *So* Propagation in Northwest Pacific

Figure 2 shows a set of typical examples of the complex records of *Po* and *So*, with very long coda, as observed at OBS stations WPAC and NM03 in the northwest Pacific. For each event, three-component records are displayed for radial (R), transverse (T), and vertical (Z) ground velocity. An instrumental response correction and a band-pass filter (2–10 Hz) were applied to emphasize the high-frequency *Po/So* phases. Since the amplitude of the vertical component is generally small at the sea bottom, the scale for the vertical component (Z) has been magnified to increase visibility. For each trace, smooth envelopes are plotted in red, so that the arrival times of *Po* and *So* phase and their broad characteristics with long coda can be clearly recognized.

2.1. Azimuthal Variation of *Po/So* Propagation

We compare OBS records at WPAC and NM03 for events in Kamchatka, the Kurile Islands and off the coast of Tohoku, Japan. At each station we use earthquakes with comparable epicentral distances and source parameters (magnitude and source depth) and find a strong dependence on the azimuth of propagation.

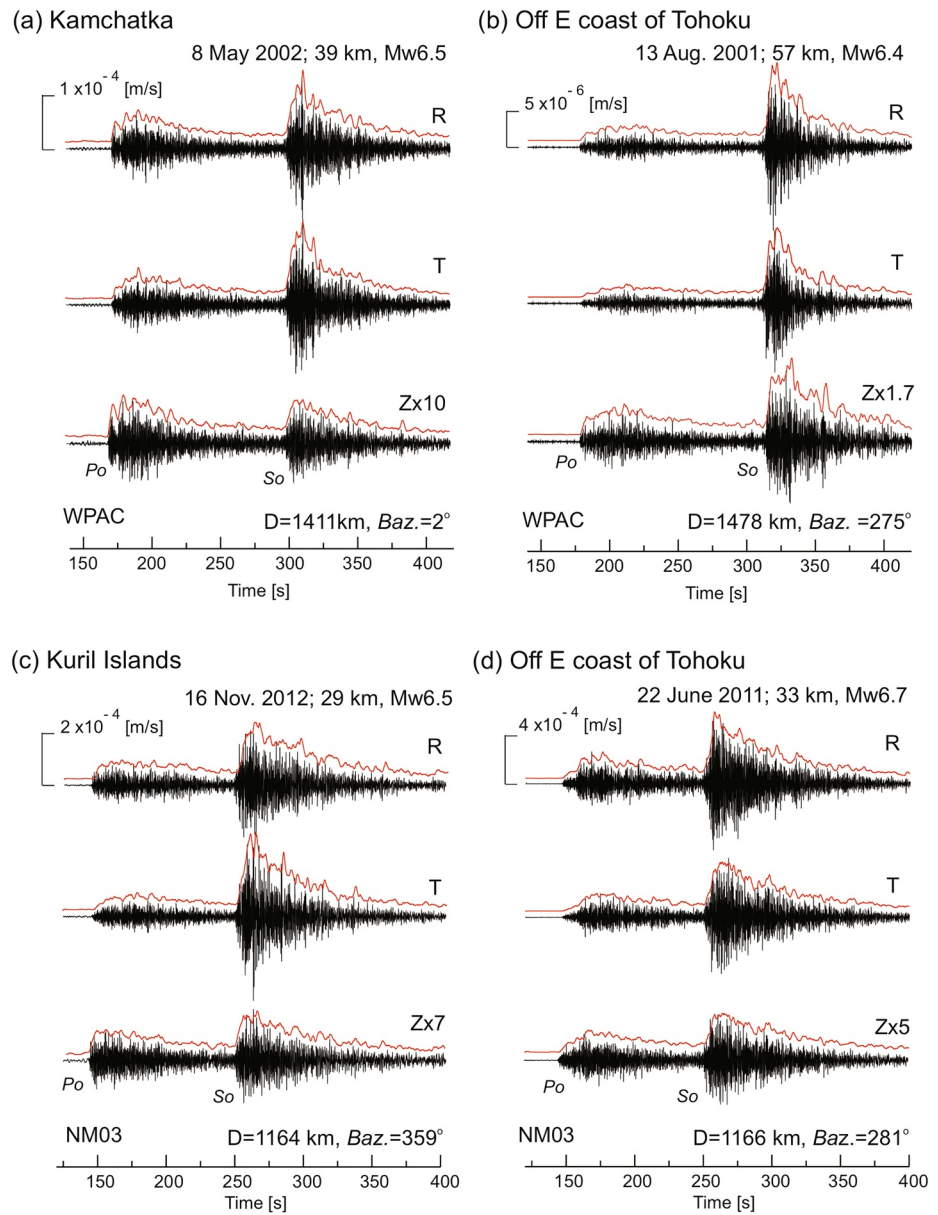


Figure 2. Comparison of three-component OBS records for radial (R), transverse (T), and vertical (Z) motions for events with similar epicentral distance. Earthquakes recorded at WPAC: (a) Kamchatka (May 8, 2002), and (b) off the east coast of Tohoku, Japan (August 13, 2001) Earthquakes recorded at NM03: (c) Kuril Islands (November 16, 2012), and (d) Off the east coast of Tohoku, Honshu, Japan (June 22, 2011). The waveforms of Z component are magnified to allow direct comparison with the horizontal components. The event and station locations are shown in Figure 1. Smooth envelopes are shown above each trace in red. Epicentral distances and backazimuths (*Baz.*) from station to source are indicated on the bottom right of each panel.

The observations from a 39 km deep Mw 6.5 earthquake in Kamchatka, to the north of WPAC at an epicentral distance of 1,411 km, show a sharp rise in the *Po* phase followed by a burst of reverberations with an interval of about 5–10 s (Figure 2a). The rapid rise of *Po* is pronounced on the Z and R components, though gentler for the T component where *Po* is generated indirectly by scattering. The propagation of *Po* is strengthened by the reverberations of *P* wave in the seawater, and the long *Po* coda (>100 s) overlaps the *So* phase. *So* is larger than *Po* on the horizontal components, but on the Z component, the amplitude of *So* is about the same as *Po*.

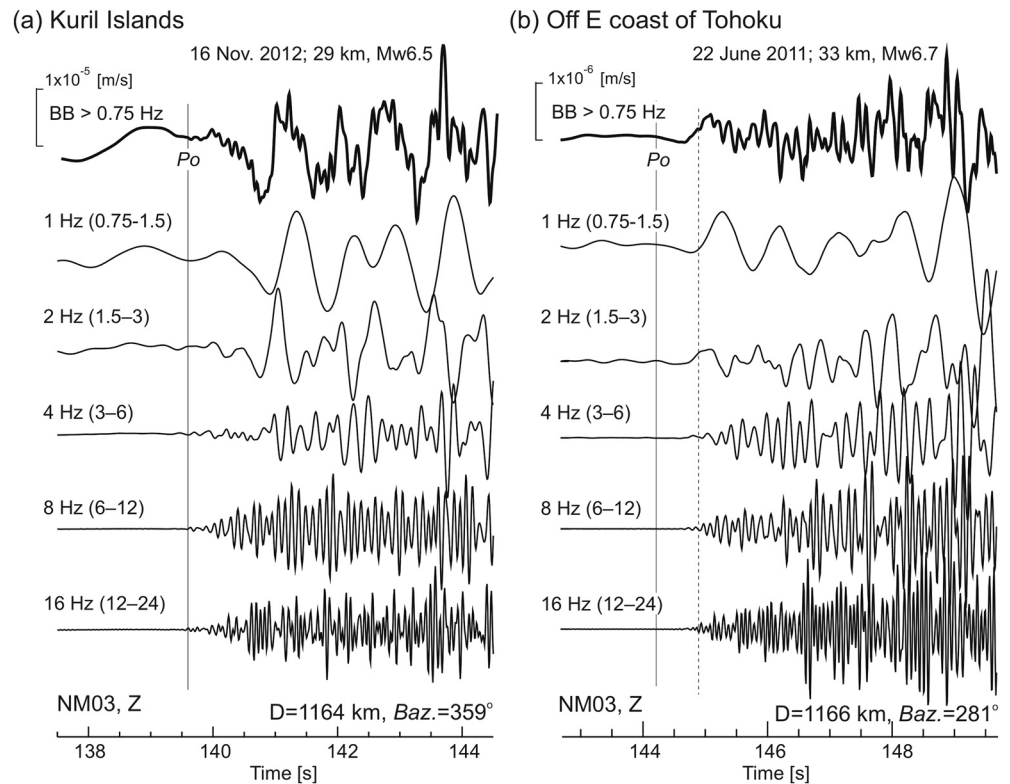


Figure 3. Broadband (top, thick line) and band-pass filtered seismograms of Z-component record of early Po , with a central frequency of 1, 2, 4, 8, and 16 Hz (numbers in parentheses indicate the passband range) for the earthquake of (a) Kuril Islands (Figure 2c), and (b) off the east coast of Honshu, Japan (Figure 2d) at station NM03. The solid vertical line indicates a weak precursor of Po , and the dashed line indicates the delay in the arrival of the high frequencies.

In contrast, for an earthquake that occurred off the east coast of Tohoku in Honshu, Japan (Figure 2b), WSW of WPAC with similar epicentral distance (1,478 km) and source parameters (depth 57 km, Mw 6.4), the observed Po shows a gentle rise with the peak amplitude delayed by more than 30 s after the initial onset. Such a long, spindle-shaped Po coda can be seen in on all three components, indicating strong scattering of high-frequency signals during propagation. Similarly, the peak amplitude of the So appears to be delayed for Z motion. However, the change in the shape of the So arrival with propagation direction is not as strong as for Po .

Similar azimuthal dependency in the Po propagation characteristics was found in the OBS records at NM03, about 400 km WSW of WPAC, for earthquakes in the Kuril Islands and off the Tohoku coast. Once again there is a sharp rise of the Po onset for the Kuril Islands earthquake (Figure 2c), and a gentle rise of Po with a long spindle-shaped coda from an event off the east coast of Tohoku (Figure 2d). Thus, the observed azimuth dependent Po (and So) propagation anomaly is not a localized effect near stations. There is some influence of the source radiation effects of inter-plate earthquakes in different subduction-zone environments (Kamchatka and Kuril Islands relative to the Japan trench) that might also affect the shape of the observed Po and So . However, the scattering of high-frequency (>2 Hz) waves in the course of long-distance propagation has the effect of almost homogenizing the radiation pattern in all directions (e.g., Takemura et al., 2015). Therefore, the observed directionality in the Po/So characters at OBS stations needs to be explained by azimuth dependent source-to-station path effects across the northwest Pacific.

2.2. Frequency Dependent Po Propagation

The changes in the shape of the Po phase on the different paths across the northwest Pacific to NM03, shown in Figure 2, are examined in detail in Figure 3. For the initial Po phase of the Z component for the events to the north and WSW, the original broad-band records are compared with the results of selective

filtering. A bandpass filter (one-pass Butterworth filter with a 2-pole cut off) was applied with central frequencies of 1, 2, 4, 8, and 16 Hz.

The Po phase that has traveled from the Kuril Islands earthquake to NM03 has a small initial arrival and the main signal shows a slight delay of about 0.3 s on all frequency components. The propagation of Po at a constant speed for all frequencies (Figure 3a) explains the sharply rising Po phase observed at WPAC and NM03 from the earthquakes to the north (Figures 2a and 2c).

In contrast, Po from the earthquake off the east coast of Tohoku, to the WSW of NM03, has a low-frequency (<2 Hz) precursor and delayed high-frequency (>4 Hz) signals by about 0.8 s (Figure 3b). This produces a weak frequency dispersion for Po , with the apparent velocity for high frequency (>4 Hz) records slower than on broadband records. A delayed Po peak more than 2.5 s after the first arrival is seen at most frequencies as part of a long spindle-shaped Po coda.

The observations of directionality in the Po/So propagation characteristics across northwest Pacific shown in Figures 2 and 3 suggest the presence of azimuthal dependence in the fine-scale heterogeneity structure of the oceanic lithosphere that largely controls the scattering and guiding properties of high-frequency Po/So signal.

2.3. Azimuth Dependent Po/So Propagation

To investigate the details of the change in Po/So shapes after propagating from sources to OBS stations across the northwest Pacific at different angles, we compare Z-component records at WPAC for shallow (<100 km) earthquakes that occurred along the Pacific subduction zones of the Pacific rim from the Aleutians to Izu-Bonin (Figure 4). We display a record section of 15 earthquakes (Mw 5.9–7.4) with epicentral distance 840–2,210 km, covering a relatively wide station-to-source backazimuth range from 62 to 223° from north. The source parameters are taken from the International Seismological Centre (ISC) catalog (Table S1 in the Supporting Information). Deeper earthquakes (depth > 150 km) were not used in this study to avoid overlapping Po and low-frequency P waves traveling through the low- Q asthenosphere.

Bandpass filtering (3–10 Hz) was applied to the observed records to remove low-frequency oceanic noise and enhance the high-frequency Po/So phases. Each trace of the record section was normalized by its maximum amplitude and aligned at the expected Po arrival time assuming wavespeed of 8.2 km/s. In Figure 4, smoothed envelopes are plotted above each trace so that azimuthal changes in the Po/So phases can be more readily appreciated. There is some influence of propagation distance on the shape of Po/So due to the strong scattering and intrinsic attenuation effects that accompany propagation, but these are expected to be weak since lithospheric attenuation is low in the northwest Pacific ($Q_p > 3,000$; $Q_s > 2,000$; Takeuchi et al., 2017). The coda tends to saturate after long-distance propagation due to the finite thickness of the heterogeneous oceanic lithosphere (about 100 km).

The results displayed in Figure 4 show significant differences in the relative properties of the Po/So phase as a function of the station-to-source backazimuth for the events. Po phases from Kamchatka to Kuril Islands earthquakes in the backazimuth range 300°–0° show a sharp rise at onset as seen in Figures 2a and 2c. These paths correspond to the direction perpendicular to the fossil magnetic anomaly pattern on the seafloor (see also Figure S1b in Supporting Information for an enlarged map). In contrast, most Po phases from the earthquakes off the east coast of Tohoku with the station-to-source backazimuth 240–270° and those from the Kamchatka and Aleutian Islands earthquakes with backazimuth 330–10° for the paths to WPAC show a very slow rise in the Po signal and exhibit spindle-shaped long codas, as seen in Figures 2b and 2d. Such azimuthal variation in the initial shape and coda is more pronounced for Po than So , probably due to the stronger interaction with shallow structure and P multiples in the seawater column.

Similar properties of the azimuthal dependence of the shape of Po/So are also found at NM03, with some spatial variations due to local structure. An equivalent section to Figure 4 is shown in Figure S1a of the Supporting Information, with a sharp Po/So rise from earthquakes in the backazimuth range between 310° to 0° and spindle-shaped Po/So for records at smaller and larger azimuths.

The orientation of the fossil magnetic anomaly at the seafloor in the northwest Pacific is consistent over the domain from the OBS to Tohoku and Kamchatka. However, there is a change in pattern between

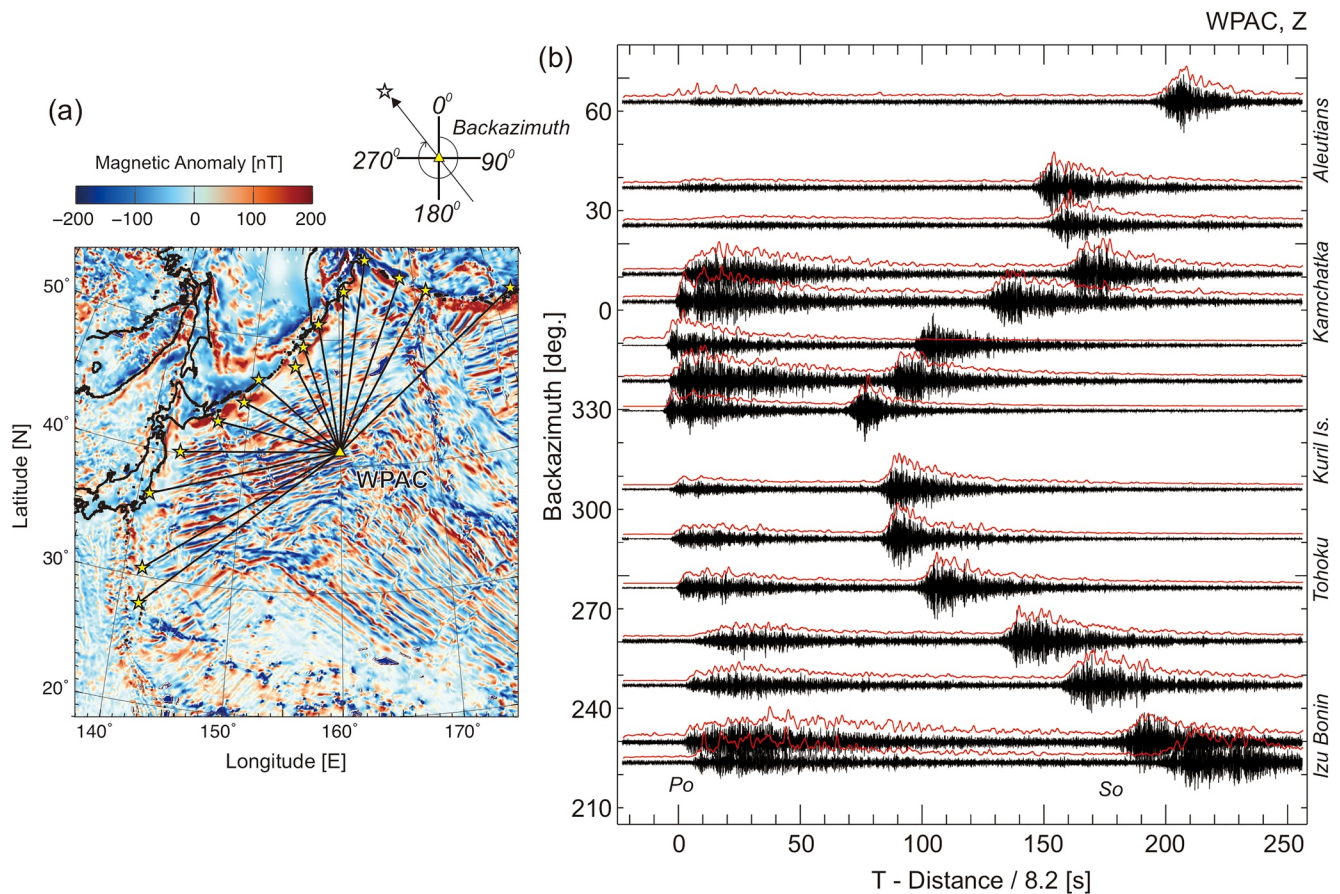


Figure 4. Record section of the Z-component of ground velocity for *Po* and *So* phases recorded at WPAC as a function of backazimuth from station to source. (a) A raypath diagram from source to station superimposed on the pattern of magnetic anomalies (Meyer et al., 2017), and enlarged version is shown in Figure S1b of the Supporting Information. (b) Plots of waveforms at station WPAC. Each trace in the record section is aligned using a P wavespeed of 8.2 km/s and normalized by the maximum amplitude. Smoothed envelopes are shown above the records in red. Also see Figure S1a of the Supporting Information for an equivalent record section for NM03.

Kamachotka and the Emperor seamount chain along 170°E. Also there is a reorientation in the south of the Izu Bonin chain (Figure 4a, also see Figure S1b). These broader scale variations in structure will also affect the apparent azimuthal dependence of *Po/So* propagation (Figure 4 and Figure S1a)

2.4. Peak Delay Time of *Po* and *So*

To quantify the change in the *Po/So* shape as a function of the azimuth of the propagation direction from source to station across northwest Pacific, the delay time of the maximum amplitude of *Po* (dT_{po}) and *So* (dT_{so}) from the first arrivals were examined from the Z-component record (as indicated in Figure 5b).

The measured peak delay times of dT_{po} and dT_{so} at the WPAC and NM03 stations are plotted in Figure 5 as a function of backazimuth from the stations to sources. At WPAC 31 earthquakes were used and 18 at NM03, with station-to-source backazimuth ranges from 200° to 65°. The minimum dT_{po} and dT_{so} occurs for backazimuths around 330–340°. The estimates of dT_{po} increase gradually away from the minimum. The delay dT_{so} is slightly smaller than dT_{po} with a broader range of smaller values between 260° and 350°. Although full azimuth coverage cannot be achieved, since there are no earthquakes southeast of the OBS, the maximum values of dT_{po} and dT_{so} are expected around backazimuths 220° and 60°, perpendicular to the backazimuth of minimum delay (330–340°).

The measured directional variations of dT_{po} and dT_{so} at WPAC and NM03 are consistent with minimum dT_{po} and dT_{so} at backazimuth 330–340°. However, the rise in dT_{po} after passing the azimuth of the

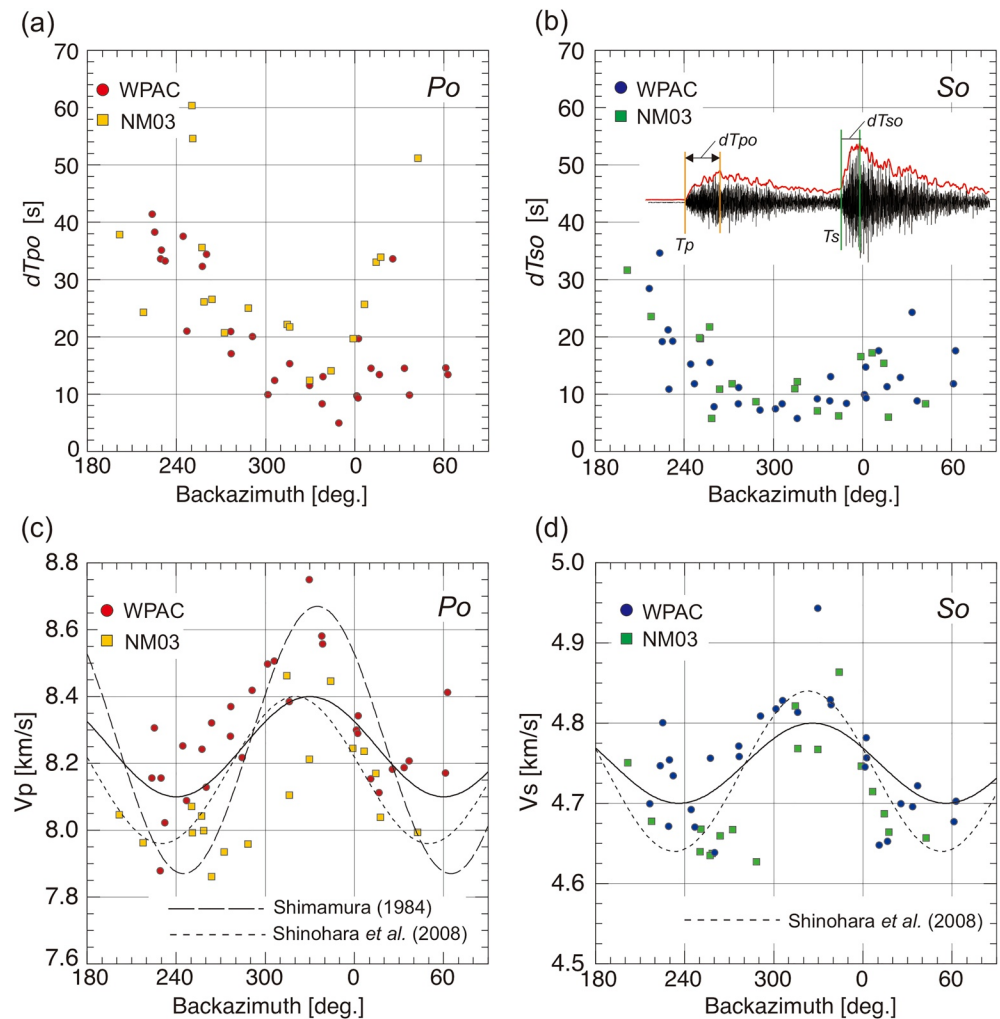


Figure 5. (a) Measured peak delay time of Po and (b) So as a function of azimuth from source to WPAC station (red and blue circles) and to NM03 station (orange and green squares). A schematic illustration of the measurement of the peak delay time is shown in the inserted figure. (c) Measured Po and (d) So wavespeed anisotropy as a function of station-to-source backazimuths. Estimates of Pn - and Sn -wavespeed anisotropy functions (fitted with least squares) are shown by solid curves with dashed curves for those from earlier studies (Shimamura, 1984; Shinohara et al., 2008).

minimum is much gentler at WPAC (red circles in Figure 5a) than at NM03 (orange squares in Figure 5a). A possible reason could be the change in the structure across the Emperor seamount chain along 170°E, as inferred from the magnetic anomaly map and ray paths shown in Figure S1b. We note that the waveguide effect associated with propagation parallel to the elongated heterogeneity would not persist along the whole raypath from sources in the Aleutians to the stations.

2.5. Po/So Wavespeed Anisotropy

The direction of propagation across the northwest Pacific that shows a sharp Po/So rise, and thus, a small peak delay time (dT_{po} and dT_{so}) is in good agreement with the direction of maximum Pn -wavespeed anisotropy determined from refraction experiments in northwest Pacific (Shimamura, 1984; Shinohara et al., 2008), frequency dispersion of surface waves (Takeo et al., 2018), and the analysis of Po/So from the earthquakes in the Pacific subduction zone (Shito et al., 2017; Takeuchi et al., 2020). The direction of the fastest Pn corresponds to the former Pacific plate motion direction before 40 Ma, N30°W, inferred from the fossil magnetic anomaly patterns on the seafloor (Meyer, 2017; Nakanishi et al., 1989; see Figure S1a of

the Supporting Information). Thus, the sharp rise in Po/So onsets appears for propagation in the direction orthogonal to the magnetic anomaly pattern, and the spindle shaped long Po/So codas appears for the parallel direction.

Po/So -wavespeed anisotropy was also confirmed from the OBS records used in this study, based on the arrival time of the band-pass (2–10 Hz) filtered Z-component records and epicentral distance, which are displayed in Figures 5c and 5d as a function of backazimuth from source to station. The estimated Po/So wavespeeds at stations WPAC and NM03 had a relatively large bias (± 0.2 km/s), probably due to site effects in the neighborhood of the stations. The estimated azimuth functions of the Po/So wavespeed from fitting a $\cos 2\theta$ azimuthal function, in the sense of least squares, are shown in Figures 5c and 5d. The result indicates that the maximum Po wavespeed occurs at backazimuth 330° and maximum So wavespeed at 326° . These directions correspond well to those from the earlier studies (Shimamura, 1984; Shinohara et al., 2008; Shito et al., 2017; Takeuchi et al., 2020).

The cause of the observed Pn -wavespeed anisotropy in oceanic lithosphere has been explained as due to preferred orientation of the axes of olivine crystals, imposed when the plate was formed at the mid-ocean ridge and during spreading over the asthenosphere (e.g., Zhang & Karato, 1995). In contrast, the observed Po/So propagation characteristics due to high-frequency wave scattering in the fine-scale heterogeneities of the oceanic lithosphere occurs due to much larger-scale anomalies of several kilometers in size (e.g., Kennett & Furumura, 2015). It would appear that the origins of both features come from the same processes during the generation and spread of the oceanic plate but are produced by different mechanisms.

3. Nature of Heterogeneity in the Oceanic Lithosphere

The observational results reveal the complexity of the characteristics of the Po and So phases propagating across the northwest Pacific, with an azimuthally varying strong-scattering environment. The patterns of variation suggest the presence of lateral variation in the fine-scale heterogeneity structure of the oceanic lithosphere.

For the northwest Pacific the properties of observed Po and So show a distinct variation with the azimuth of the path, controlled by the location of the earthquake sources in the subducting Pacific plate. The oceanic lithosphere in this region was originally created at a fast-spreading ridge (around 6 cm/yr half-spreading rate) and so we seek clues for the likely character of the detailed 3-D heterogeneity distribution from a modern analogue, the East Pacific Rise. Along the axis of this mid-ocean ridge, the behavior is segmented into portions around 30 km long separated by transform faults, jogs in the ridge direction or overlapping ridge segments (e.g., Marjanović et al., 2015, 2018). In the perpendicular direction (i.e., plate spreading direction) distinct topographic features occur at 1–2 km intervals, associated with abyssal hills and deep-seated faulting of the newly formed oceanic crust (e.g., Buck et al., 2005; Harding et al., 1993). Such near-surface processes are strongest near the mid-ocean ridge, but their influence persists through the lifetime of the oceanic lithosphere. Such faults can be reactivated when plate bends in the outer-rise of the subduction zone (Fujie et al., 2018; Kita & Ferrand, 2018) and cause deep-focus earthquakes in the subducting slab (Li et al., 2018). The scales of variation associated with these shallow processes will be of the order of a kilometer or so.

A further set of processes associated with flow in the mantle and accretion onto the oceanic lithosphere come in from the base of the lithosphere. The magma chamber along the axis of a fast-spreading ridge extends for tens of kilometers, this scale is much larger than the spacing of surface topographic features that reflect cross-ridge processes. Away from the ridge, mantle flow can be expected to bring elongate pods of melt into contact with the base of the thickening lithosphere producing a complex heterogeneous zone (Hirschmann, 2010), whose mineralogical character will vary with the age of the plate. The associated scale lengths will be larger than for the near-surface processes typically 5 km or more.

Figure 6 shows the way in which these heterogeneity inducing processes interact in 3-D near the mid-ocean ridge and resultant for ancient oceanic lithosphere. In each block, features are shown at true

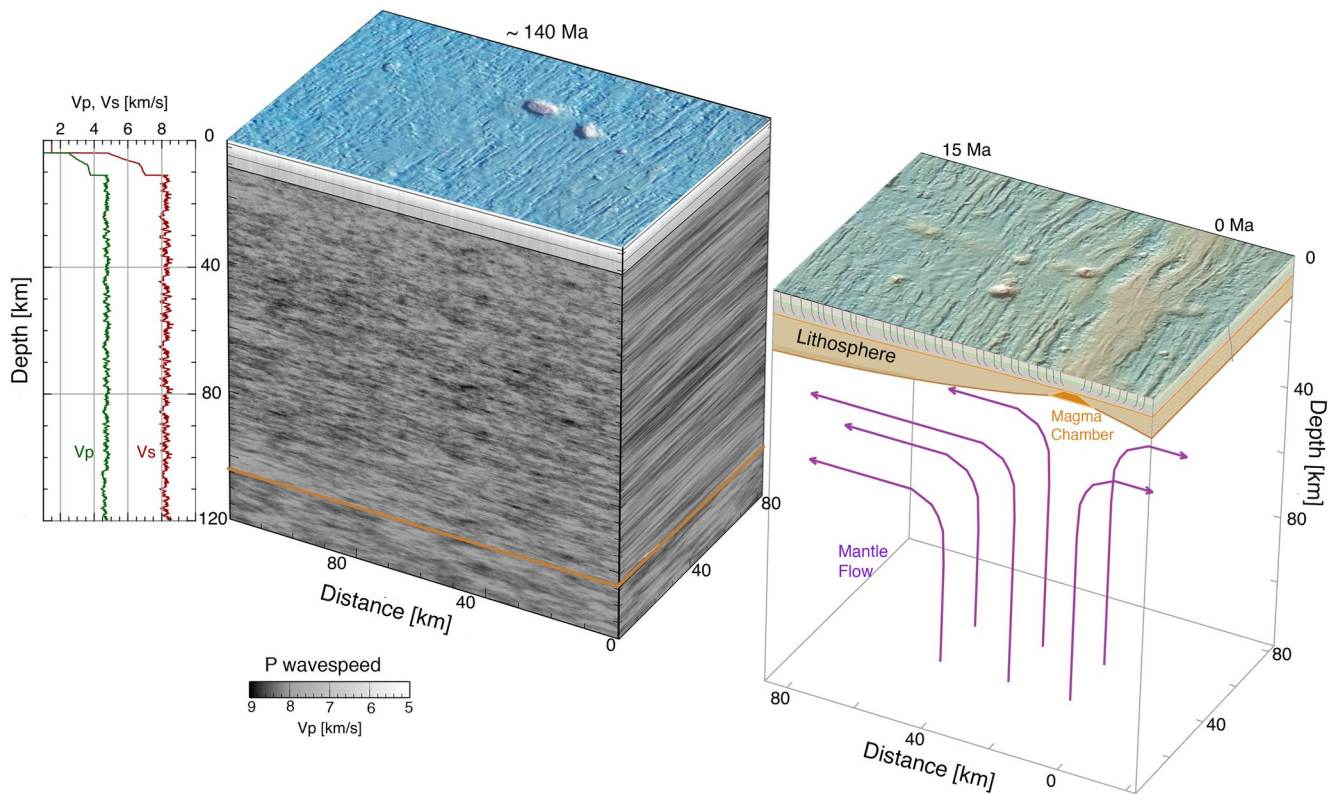


Figure 6. Three dimensional representation of the generation of heterogeneity near a fast-spreading ridge, showing surface topography and associated spreading processes on the right, and mature lithosphere at the left, together with representative one dimensional wavespeed profiles. The variations in seismic wavespeed were produced by the superposition of a fine-scale variation perpendicular to spreading that diminishes with depth, combined with a somewhat larger scale variability associated with basal processes that increase with depth to the base of the lithosphere (indicated by an orange line at depth of 112 km). In each case the variability along the former spreading axis has a correlation length of 20 km. Topography is from the Marine Geoscience Data System bathymetric data (Ryan et al., 2009) for the East-Pacific Rise at 8.5°–10.0°N.

Table 1
Heterogeneity Parameters in the Crust (C), Lithosphere (L), and Asthenosphere (A) for 3-D Model Using a Von Kármán Stochastic Random Distribution With Different Correlation Distances in 3-D and Amplitude of Standard Deviation of Heterogeneity (ϵ)

Model	Zone	Horiz. correl. dist. ax, ay [km]	Vert. Correl. Dist. az [km]	Rms. fluctuation ϵ [%]
(a)	C	20, 0.25	5	2
	L	20, 1	0.5	0.5–1.5
		20, 5	0.5	1.5–0.5
A	10, 5	1	2	
(b)	C	10, 0.25	5	2
	L	10, 10	0.5	2
		10, 5	1	2
A	10, 5	1	2	
(c)	C	40, 0.25	5	2
	L	40, 1	0.5	0.5–1.5
		40, 5	0.5	1.5–0.5
	A	10, 5	1	2

vertical-to-horizontal scale. We here illustrate a stochastic heterogeneity model combining both near-surface and basal effects with different scales of variation. We impose a correlation length of 20 km in the direction of the former spreading axis for both stochastic components (Table 1a). In the perpendicular direction, we introduce heterogeneity due to surface processes with a correlation length of 1 km diminishing in amplitude from 1.5% at the crust-mantle boundary to 0.5% at the base of the lithosphere. The second component from basal processes has a correlation length of 5 km and builds from 0.5% amplitude at the base of the crust to 1.5% at the lithosphere-asthenosphere boundary, comparable to that employed by Kennett and Furumura (2015). For a broad range of azimuths around the axis of the longer correlation length of heterogeneity the apparent distribution is comparable to $a_h = 10$ km considered in 2-D simulations (Furumura & Kennett, 2005, 2008; Kennett & Furumura, 2015).

The interaction of these two different scales of heterogeneity has an interesting effect with a distinctive banding arising around 60 km depth, where a number of studies have indicated the presence of an oceanic G-discontinuity (see, e.g., Auer et al., 2015). Changes in the nature of the heterogeneity distribution with depth have the possibility of inducing effects similar to the presence of a discontinuity, particularly in the mid-lithosphere environment (e.g., Kennett et al., 2017).

4. 3-D FDM Simulation

We undertake 3-D FDM simulations of seismic wave propagation to show that the azimuthal differences in the Po/So propagation behavior in the northwest Pacific are mostly associated with strong scattering in the 3-D heterogeneous oceanic lithosphere. The finer-scale details of the actual oceanic structure of the northwest Pacific subduction zones in 3-D are still difficult to extract even with modern high-density seismic experiments. So, we employ a layered structure with a laterally heterogeneous stochastic random heterogeneity model to investigate the effect of fine-scale heterogeneity structure in the crust, lithosphere, and asthenosphere on Po/So propagation. Thus, this simulation aims to demonstrate major characteristics in the variation of the Po/So shape with respect to the heterogeneity distribution, but does not attempt to provide a full match to observed waveforms. The base model is isotropic, and we superimpose stochastic random fluctuations in 3-D to the averaged P - and S -wavespeeds and density model of the northwest Pacific.

With the use of stochastic heterogeneity we summarize the properties of the heterogeneity distribution with a just a few parameters. Numerical simulation can only use one representative structure, but numerical tests indicate that the properties of the scattering wavefield are robust. In particular, the envelope of seismograms shows little dependence on the specific choice of random seed in generating the stochastic random heterogeneity model.

4.1. Simulation Model

The area of simulation used is 1925.12 km by 1925.12 km in the horizontal directions and 128 km in depth, discretized with a 0.08 km grid size, as shown in Figure 7. Large scale simulations were conducted with parallel 3-D FDM simulation (Maeda et al., 2017) using 2,048 nodes of the Oakforest-PACS computer at the Supercomputer Center of the University of Tokyo. The simulations required 80.4 TByte of computer memory and 14.4 h CPU time to model 420 s of wave propagation with 120,000 time-steps.

The velocity profile with depth for the northwest Pacific is based on that of Shinohara et al. (2008) and Kodaira et al. (2014) from reflection and refraction experiments and travel time analysis of regional and teleseismic records. The model was extended to the depth of the asthenosphere using the $ak135$ model (Kennett et al., 1995), with a slight positive velocity gradient from the crust-mantle boundary to the middle of the lithospheric mantle which connects to negative gradient below down to the base of the lithosphere (Figure 7b). In order to carry out high frequency modeling to 4.8 Hz, we have removed a thin (0.4 km), very low S -wavespeed ($V_s = 0.2$ km/s) layer immediately beneath the seafloor from the model of Kodaira et al. (2014). Based on a 2-D FDM simulation with a finer (0.02 km) grid, we confirmed that such a thin layer has only a minor effect on Po/So propagation, especially for Z component, though it may cause large Po -to- S conversion at the seafloor for R motion (Tonegawa et al., 2018, see, Figure S2 in Supporting Information).

The fine-scale heterogeneity of the crust, lithosphere, and asthenosphere were modeled using a von Kármán stochastic random distribution functions which were superposed on the 1-D background velocity and density following Kennett and Furumura (2013). A simplified model of heterogeneity in the oceanic crust employs vertically elongated dykes with $ax = 20$ km, $ay = 0.25$ km, and $az = 5$ km and 2% standard deviation to the background P - and S -wavespeeds and 1.6% for density. The heterogeneity in the lithosphere was assumed to consist of two components; the first has a short correlation distance of $ay = 1$ km in the direction perpendicular to the fossil magnetic anomaly diminishing in amplitude from 1.5% to 0.5% from top to bottom of the oceanic mantle; and the second has a longer correlation distance ($ay = 5$ km) growing in amplitude from 0.5% to 1.5% with depth. Both lithospheric heterogeneity components have correlation distance $ax = 20$ km along the longer axis of heterogeneity and $az = 0.5$ km in depth (Table 1a). Such multi-scale heterogeneity structure in the oceanic lithosphere can be effective in guiding Po/So and so maintaining Po/So energies over long distances. The laterally elongated structures is thought to produce a scattering waveguide in the lithosphere with strong azimuthal variations. The heterogeneities in the asthenosphere were set with correlation distances of $ax = 10$ km and $ay = 5$ km, and $az = 0.5$ km, and standard deviation of 2% for P and S -wavespeeds and 1.6% for density.

Anelastic attenuation coefficients for P and S waves (Q_p and Q_s) were set in the simulation model for oceanic crust with $Q_p/Q_s = 500/300$, lithosphere with $Q_p/Q_s = 3,000/2,000$, and asthenosphere with

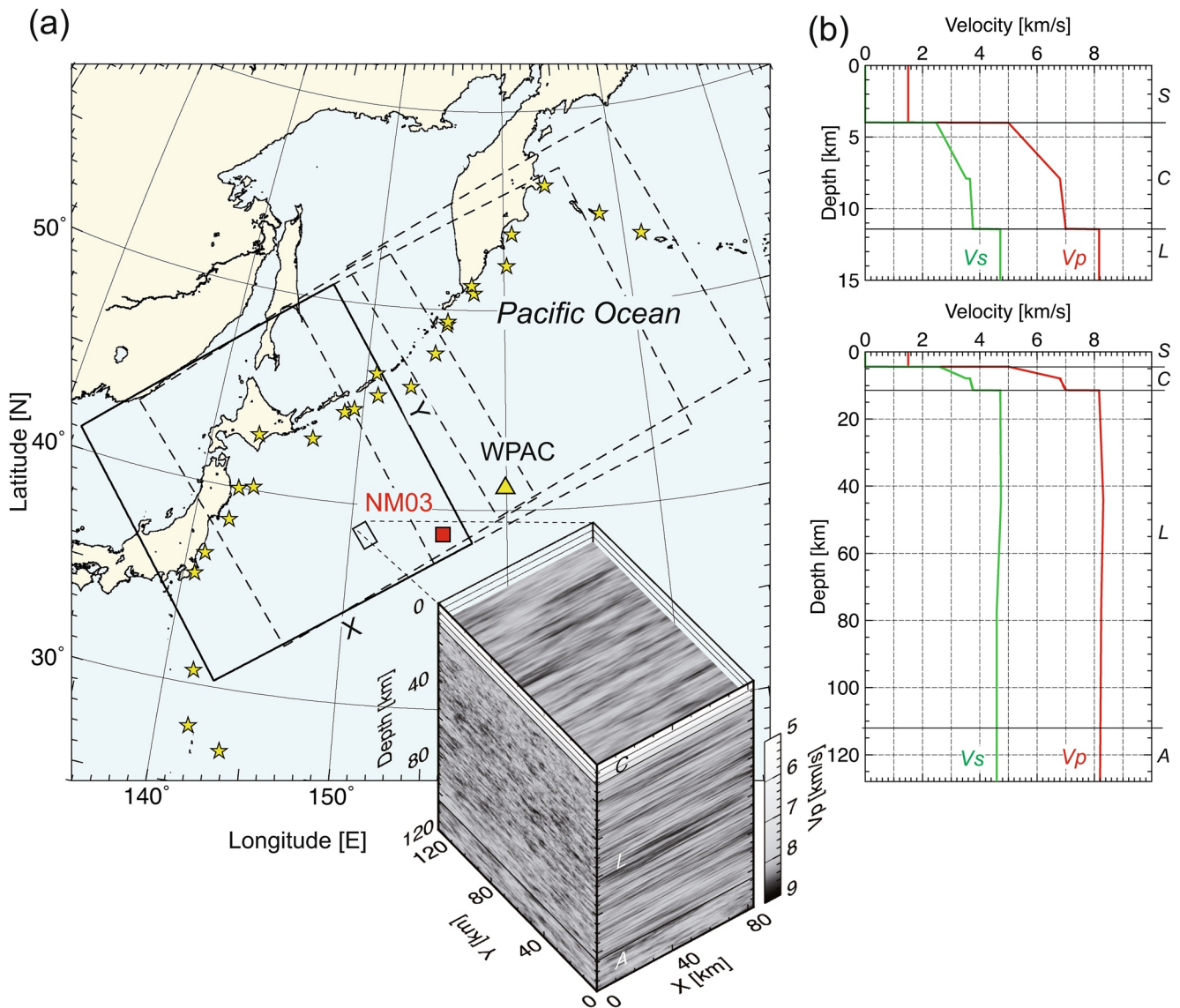


Figure 7. (a) The black square outlines the area used for three dimensional (3-D) finite-difference method simulation for wave propagation from a set of sources (yellow stars) to station NM03; a 3-D view of a segment of P -wavespeed model with fine-scale heterogeneity is shown. This simulation can also examine the wave propagation from the earthquakes in northeast, and from earthquakes to station WPAC, taking into account geometrical symmetry (dashed squares). (b) 1-D P - and S -wavespeed model used in this simulation of the northwest Pacific with seawater (S), crust (C) extracted from Kodaira et al. (2014) removing a thin sedimentary layer just beneath the seafloor, and lithosphere (L) and asthenosphere (A) based on *ak135* (Kennett et al., 1995) with a small velocity gradient in the lithosphere.

$Q_p/Q_s = 450/300$. We have adopted a higher Q value for the asthenosphere than the estimates from Booth et al. (2014) ($Q_p = 128\text{--}165$) and from Takeuchi et al. (2017) for northwest Pacific ($Q_s = 50\text{--}100$), so that simulations may sustain significant P_0 and S_0 for large distances. The relatively low Q_p/Q_s ratio ($3/2$) adopted in this simulation model includes relatively larger bulk damping in the simulated wavefield. The structure was covered by a 4 km thick layer of sea water ($V_p = 1.5$ km/s, $V_s = 0$ km/s) with a very high Q_p (50,000).

A seismic point source was placed in the upper corner of the simulation model at a depth of 35 km, using a combined explosive and torque source with a source-time function of 0.217 s duration to simulate seismic waves below 4.7 Hz. This source radiates P and S waves uniformly in all directions, so the effect of P/S radiation patterns can be ignored.

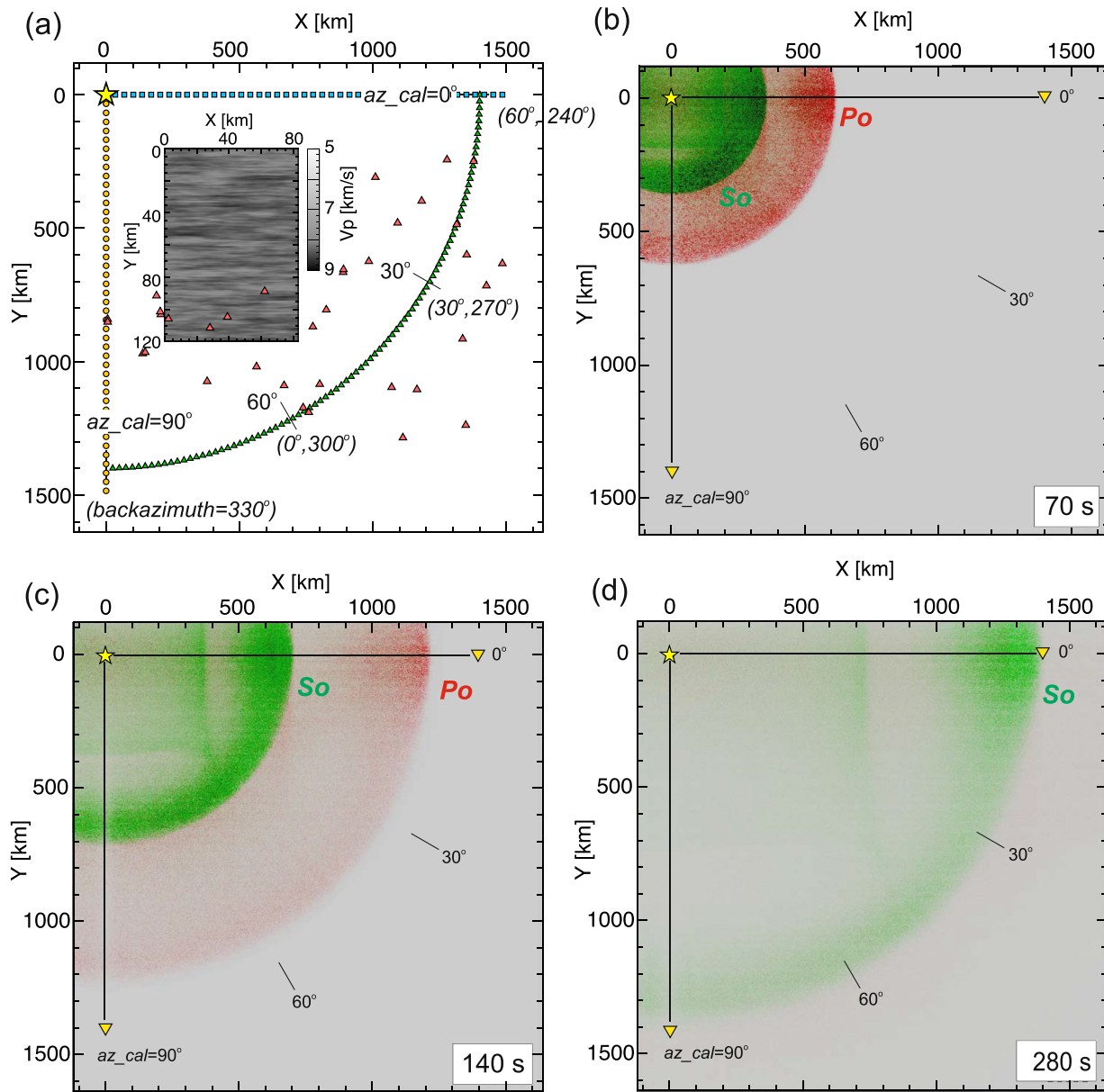


Figure 8. (a) Configuration of the three dimensional finite-difference method simulation model for a top view of the source (35 km below surface) and stations at sea bottom (blue squares, yellow circles and green triangles). The azimuth angle ($az_cal = 0-90^\circ$) is defined clockwise from the X direction of the simulation model, corresponding to longer axis of laterally elongated fine-scale heterogeneity. The corresponding locations of the OBS stations (WPAC and NM03) and epicenters in the simulation model are indicated by stars and red triangles, respectively. The angles in the parentheses indicate the corresponding actual backazimuths from source to station in the northwest Pacific. (b–d) Snapshots of seismic wavefield at sea bottom, displaying P (red) and S wavefield (green) at 70, 140, and 280 s after the earthquake initiation.

4.2. Simulation Results

The result of a 3-D FDM simulation for Po/So propagation in the heterogeneous oceanic structure is shown in Figure 8, with snapshots of P and S wavefield at the seafloor after 70, 140, and 280 s from the earthquake initiation; the wavefield is separated into P (red) and S (green) components by taking the divergence and curl of the 3-D wavefield.

The first frame of the snapshot shows P and S wavefronts radiating isotropically from the source and propagating in the heterogeneous structure by multiple scattering (70 s). We introduce the azimuth az_cal , calculated clockwise from the direction parallel to the elongated heterogeneity (X -direction) of the simulation

model, which needs to be distinguished from the station-to-source backazimuth in the actual geometry of the northwest Pacific.

After long-range propagation, the initially isotropic wavefronts of P and S waves are significantly modified with a strong concentration of Po/So energy and long codas in the X direction ($az_cal = 0^\circ$) parallel to the longer axis of the heterogeneity distribution (140 and 280 s frames). In the X direction, a weak, low-frequency precursor forms in the Po wavefront due to multiple diffraction of seismic waves along elongated fine-scale heterogeneity of a quasi-lamina, after which large and long high-frequency P coda follows (see, 140 s frame). Such a low-frequency head wave can be interpreted as a superposition of refracted waves traveling through slow-to-fast wavespeed interfaces in the quasi-lamina (Furumura & Kennett, 2008), and has also been denoted as a “tunneling wave” (Fuchs & Schulz, 1976). The range of azimuths where low-frequency head wave and subsequent large, high-frequency energy concentration occur depends on the strength of the heterogeneity, and narrows for a larger standard deviation of heterogeneity (see, Furumura & Kennett, 2008, for details). In the X direction, a long Po/So coda is formed after multiple scattering in the waveguide.

In general, the amplitudes of P and S waves attenuate more rapidly than $1/r$ at a distance r because the wavefront of seismic wave spreads spherically in 3-D, and amplitude is further reduced by the influence of intrinsic attenuation (Qp and Qs) in particularly at high frequencies. However, in the scattering waveguide formed by the quasi-lamina structure, geometrical spreading within a certain range parallel to the elongated heterogeneity can become less than $1/r$, and large amplitudes can be retained for substantial distances by energy captured within the scattering waveguide.

In contrast, in the propagation outside the scattering waveguide, the amplitude of the seismic waves decreases rapidly with distance due to the geometrical spreading and intrinsic attenuation. The attenuation of Po and So is strong in the direction of incidence almost perpendicular to the quasi-lamina structure, and multiple scattering within the structure maintains sharp Po/So rises over large distances. The snapshots in the 140 and 280 s frames show attenuated Po/So signals traveling in this direction (Y direction; $az_cal = 90^\circ$), in contrast to the large contribution in the X direction ($az_cal = 0^\circ$).

4.3. 3-Component Records

Figure 9 displays simulated three-component velocity records at the sea bottom for an epicentral distance of 1,400 km, demonstrating the difference in the Po/So shape in propagation along the direction perpendicular (Figure 9a) and parallel (Figure 9b) to the longer axis of laterally elongated heterogeneity of oceanic lithosphere. Since the simulation results might include numerical dispersion of high-frequency signals after long-distance propagation that could vary with the angle to the FDM grid configuration, we compare seismograms of $az_cal = 0^\circ$ and 90° to have similar effects.

As compared with observations at similar distances (Figure 2), the results are in good agreement with the major characteristics of the observed Po/So shapes with respect to the propagation direction across northwest Pacific. Simulated waveform with perpendicular propagation to the elongated heterogeneity (Figure 9a; $az_cal = 90^\circ$) show a sharply rising Po/So followed by a burst of energy on the R and Z components as in the observation (Figure 2a). Further, the simulated waveform for a path parallel to the elongated heterogeneity (Figure 9b; $az_cal = 0^\circ$), reproduces the observed gently rising Po/So onset with long spindle-shaped coda (Figure 2b) very clearly.

The amplitude of simulated Po in both propagation directions is smaller than in the observations. This difference probably arises because of the absence of a sediment layer in the simulation model (see, Figure S2 for detail) and the relatively low Qp/Qs ratio used in this simulation. The amplitude of Po on the T component in both propagation direction is slightly smaller than that in R and that of the observed record. This difference suggests that the present simulation underestimates the full range of scattering effects, probably due to lack of seafloor topography and moderate-scale heterogeneities. Topographic scattering can have a major contribution to the homogenization of P -wave energy among the three components of motion (Take-mura et al., 2015).

Band-pass filtered Z-component seismograms for the early part of the Po phase are compared in Figure 10, to demonstrate frequency-dependent propagation properties in different directions across laterally varying

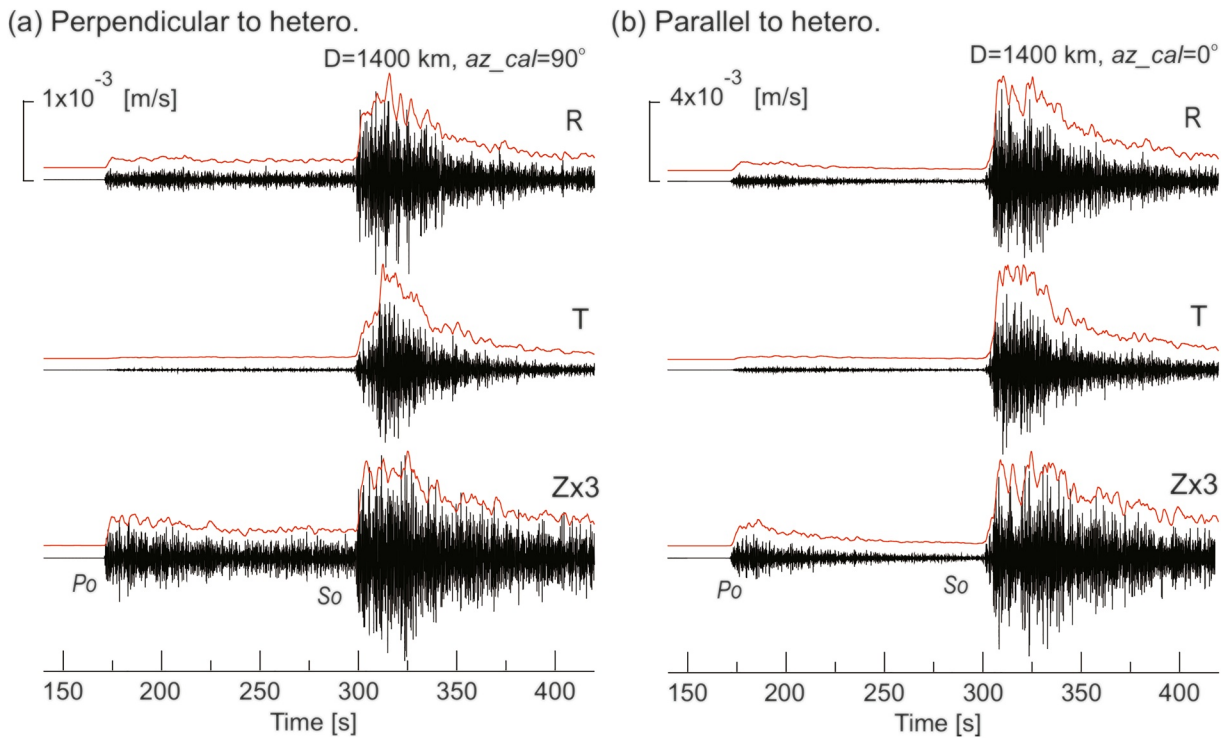


Figure 9. Records for R, T, and Z component ground velocity obtained by three dimensional finite-difference method simulation at epicentral distance of 1,400 km and in the direction (a) perpendicular to laterally elongated heterogeneity ($az_cal = 90^\circ$, see, Figure 8 for station location), and (b) parallel to this ($az_cal = 0^\circ$). A smooth envelope for each trace is shown in red.

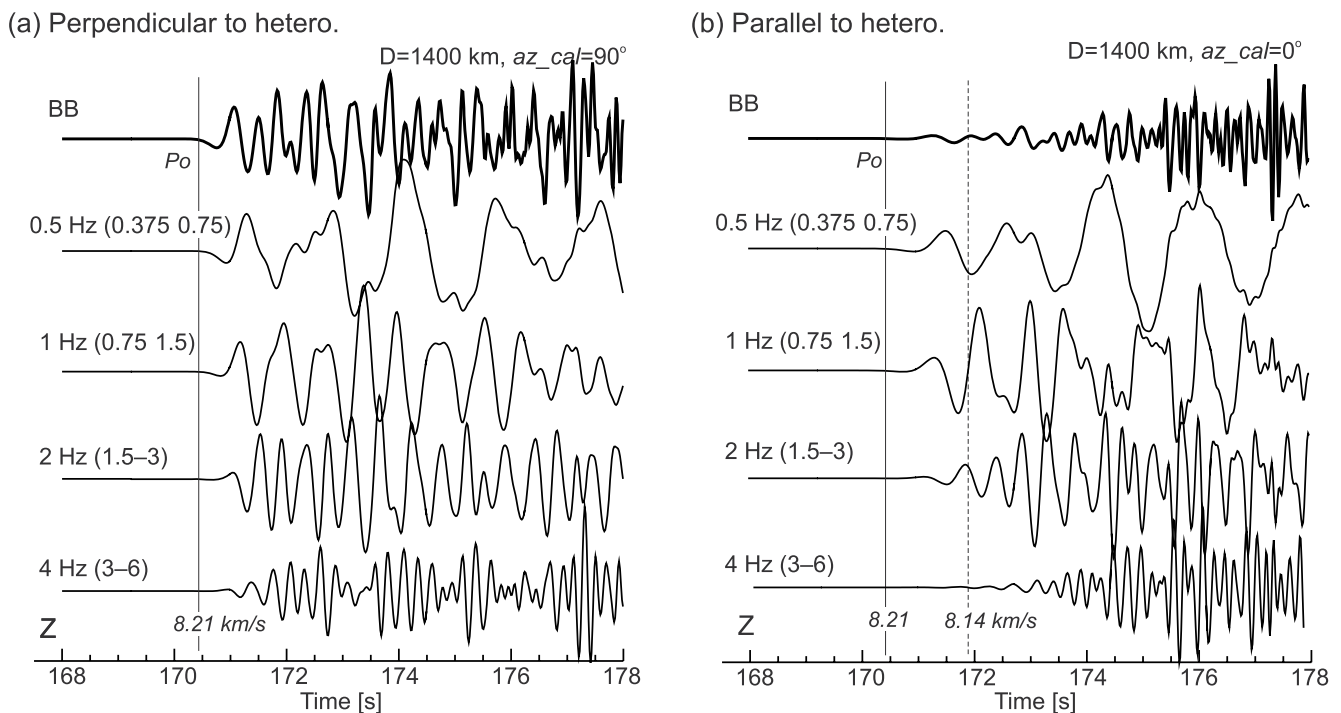


Figure 10. Band-pass filtered Z-component records of the simulated early Po segment with central frequencies of 0.5, 1, 2, and 4 Hz, and unfiltered broadband (BB) waveform recorded at epicentral distance of 1,400 km and in the direction (a) perpendicular to laterally elongated heterogeneity ($az_cal = 90^\circ$), and (b) parallel to heterogeneity ($az_cal = 0^\circ$) (see Figure 8 for station locations).

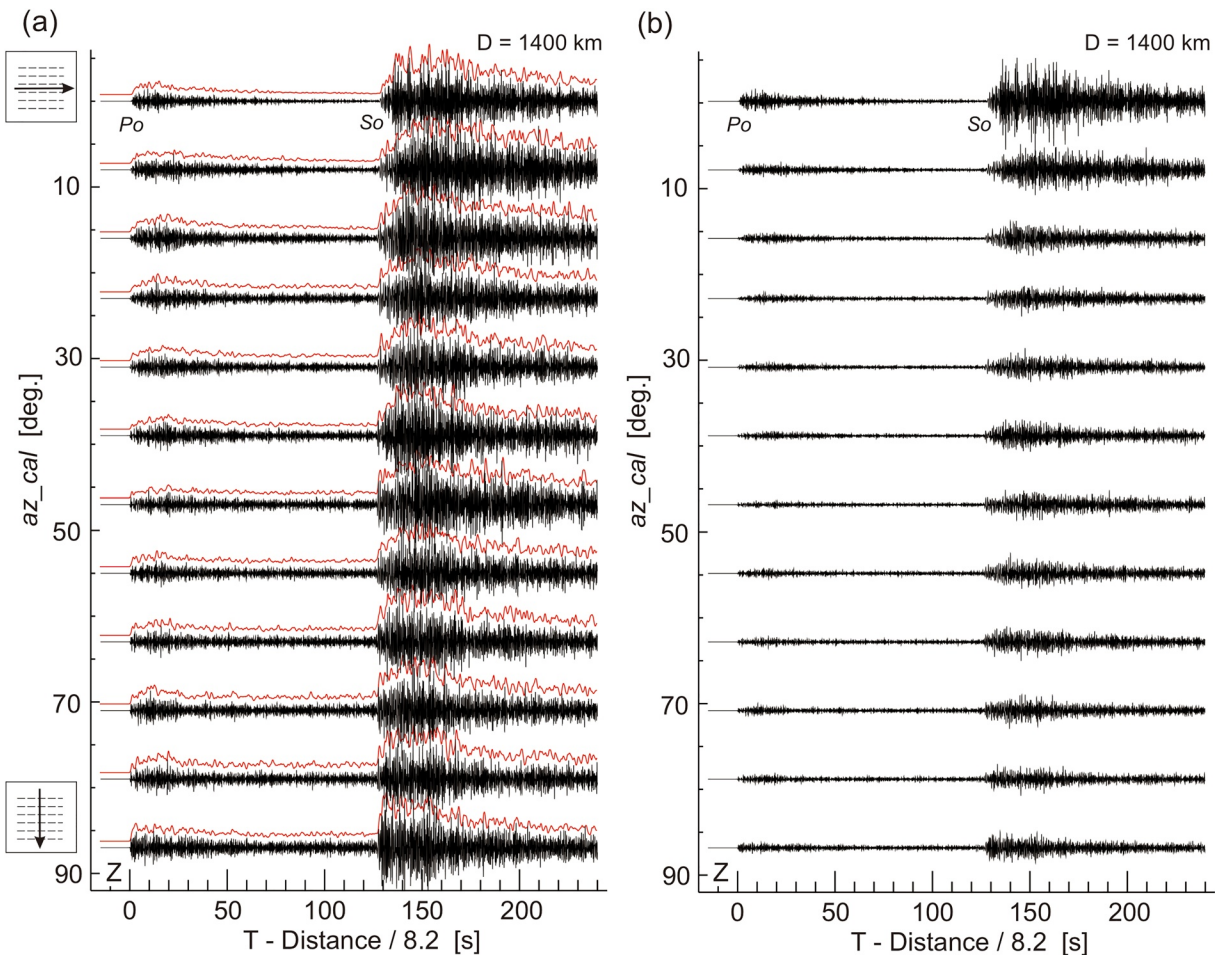


Figure 11. (a) Z-component record section and envelope at distance of 1,400 km and as a function of the azimuth angle (az_cal) of seismic wave incidence with respect to the longer axis of laterally elongated heterogeneity distribution in the simulation model; $az_cal = 0^\circ$ and 90° correspond to parallel and perpendicular direction to the elongated heterogeneity, respectively. A schematic diagram the Po/So propagation angle with respect to the longer axis of the heterogeneity distribution is shown on the left. Each trace is normalized by its maximum, and (b) a true-scale plot is shown at the right.

heterogeneous lithosphere. As in the observed records (Figure 3a), the simulated waveforms showed a weak frequency dispersion of Po with a low-frequency (<1 Hz) precursor and much delayed high-frequency (>4 Hz) components when Po travels parallel to the laterally elongated heterogeneity structure (Figure 10b). Accordingly, the estimated Po wavespeed for high frequency (4 Hz) is about 1% slower (8.14 km/s) than for low frequency (8.21 km/s for 0.5 Hz.), resulting in an apparent Po wavespeed anisotropy in this direction for long distance passage in the scattering waveguide. In contrast, in the perpendicular direction to the elongated heterogeneity, all frequencies of Po propagate at the same wavespeed and maintain a sharp Po pulse (Figure 10a).

4.4. Azimuthal Dependent Po/So Shape

Figure 11 shows a record section of the simulated Z-component velocity as a function of azimuth in the simulation domain (az_cal) at an epicentral distance of 1,400 km. Each trace in the record section is normalized by its maximum amplitude so that the relative change in the Po/So shape can be seen for propagation at different angles. To the right (Figure 11b) waveform plots with a common scale are shown, demonstrating the generation of a strong scattering waveguide in the direction parallel to the elongated heterogeneity ($az_cal = 0^\circ$).

The azimuthal dependence of *Po/So* shape in the simulation results is consistent with the observed records shown in Figure 4. In the propagation parallel to the heterogeneity ($az_cal = 0^\circ$), which corresponds to the station-to-source backazimuth of 240° or 60° in the northwest Pacific, the rise of *Po* onset is slow, and the maximum amplitude is delayed 20–40 s after the initial motion. Then, a very long *Po* coda continues for more than 120 s almost overlapping with *So*. The spindle-shaped long *Po* coda with a much delayed peak develops by multiple forward scattering parallel to the elongated fine-scale heterogeneity. The attenuation of *Po* and *So* traveling through the scattering waveguide is very weak as the trapping of high-frequency signals within the quasi-lamina results in lower geometrical attenuation, and a large signal is maintained for long distances. On the other hand, when *Po/So* propagates across the scattering waveguide at a large angle of incidence ($az_cal > 45^\circ$), the scattering waveguide effects are much reduced and the *Po/So* keeps a sharp onset but the amplitude decrease steadily with propagation distance. In this direction, *Po/So* propagates nearly perpendicular to the elongated heterogeneity, causing multiple forward and backward reflections, resulting in a burst of signals that maintains approximately the same amplitude for a long time.

4.5. *Po/So* Peak Delay Time

The sharpness of the simulated *Po/So* rise as a function of az_cal was investigated by examining the peak delay times of *Po* and *So* in the Z-component waveforms (Figure 12Aa), which are compared with the observations from the northwest Pacific (Figures 5a and 5b). The angle az_cal ($=0^\circ$ – 90°) in the simulation domain has been converted to the actual station-to-source backazimuth, taking into account the positional relationship between the simulation model and the source-to-station geometry in the northwest Pacific (see, Figures 7 and 8).

The multi-scale heterogeneous model provides a good representation of the observed *Po* and *So* delay time changes as a function backazimuth from source to stations; the *Po* and *So* peak delay time (dT_{Po} and dT_{So}) is minimized at backazimuth of about 330° (i.e., the direction perpendicular to the laterally elongated heterogeneity) and increases rapidly as the propagation diverges from this angle. The dT_{So} obtained by the simulation is slightly larger than the observed values, possibly because the scattering intensity in the present simulation model (2% standard deviation) may be slightly larger for *S* wave, coupled with the effect of numerical dispersion of FDM simulation after large distance propagation which is larger for *S* that has a shorter wavelength than *P*.

For reference, the results for the preferred heterogeneity structure are compared with a simulation using an isotropic heterogeneity ($ax = ay = 10$ km) structure in horizontal direction and maintaining other parameters ($az = 0.5$ km, and standard deviation of 2%; Table 1b) (Figure 12Ab). This horizontally isotropic case is an extension of the conventional 2-D stochastic heterogeneity model (Kennett & Furumura, 2005) without azimuthal variations. The simulated Z-component record sections are compared in S3 of the Supporting Information. The results show that the *Po* delay time for the isotropic case is significantly underestimated at all azimuths, and that there is no minimum peak delay time at any particular azimuth. We also examined another heterogeneity model with much-elongated heterogeneity structure ($ax = 40$ km, see Table 1c), resulting in a slightly larger *Po* and *So* delay time and sharper minimum delay peaks (Figure 12Ac). However, differences from the results for the original ($ax = 20$ km) structure (Figure 12Aa) are very small, this means that propagation of *Po/So* is less sensitive to further changes in ax beyond a certain scale (>20 km). These comparisons validate the effectiveness of the present heterogeneity model for the northwest Pacific lithosphere as an explanation of the observed azimuthal variation of *Po/So* propagation characteristics.

4.6. Attenuation Functions of *Po/So*

The presence of the laterally elongated heterogeneity produces azimuthally varying guiding and attenuation of *Po/So*. In Figure 13 we plot the maximum *Po* amplitude on the Z component and *So* on horizontal components as an azimuthal function of az_cal in the simulation domain (see Figure 8). We use the 3-D FDM results at epicentral distances of 600, 1,000, and 1,400 km.

A strong *Po/So* waveguide effect appears for propagation nearly parallel to the elongated heterogeneity distribution ($az_cal < 20^\circ$). The *Po* and *So* amplitudes increases sharply as az_cal approaches 0° . The amplification of *Po* and *So* in this direction relative to those in the perpendicular direction ($az_cal = 90^\circ$) increases

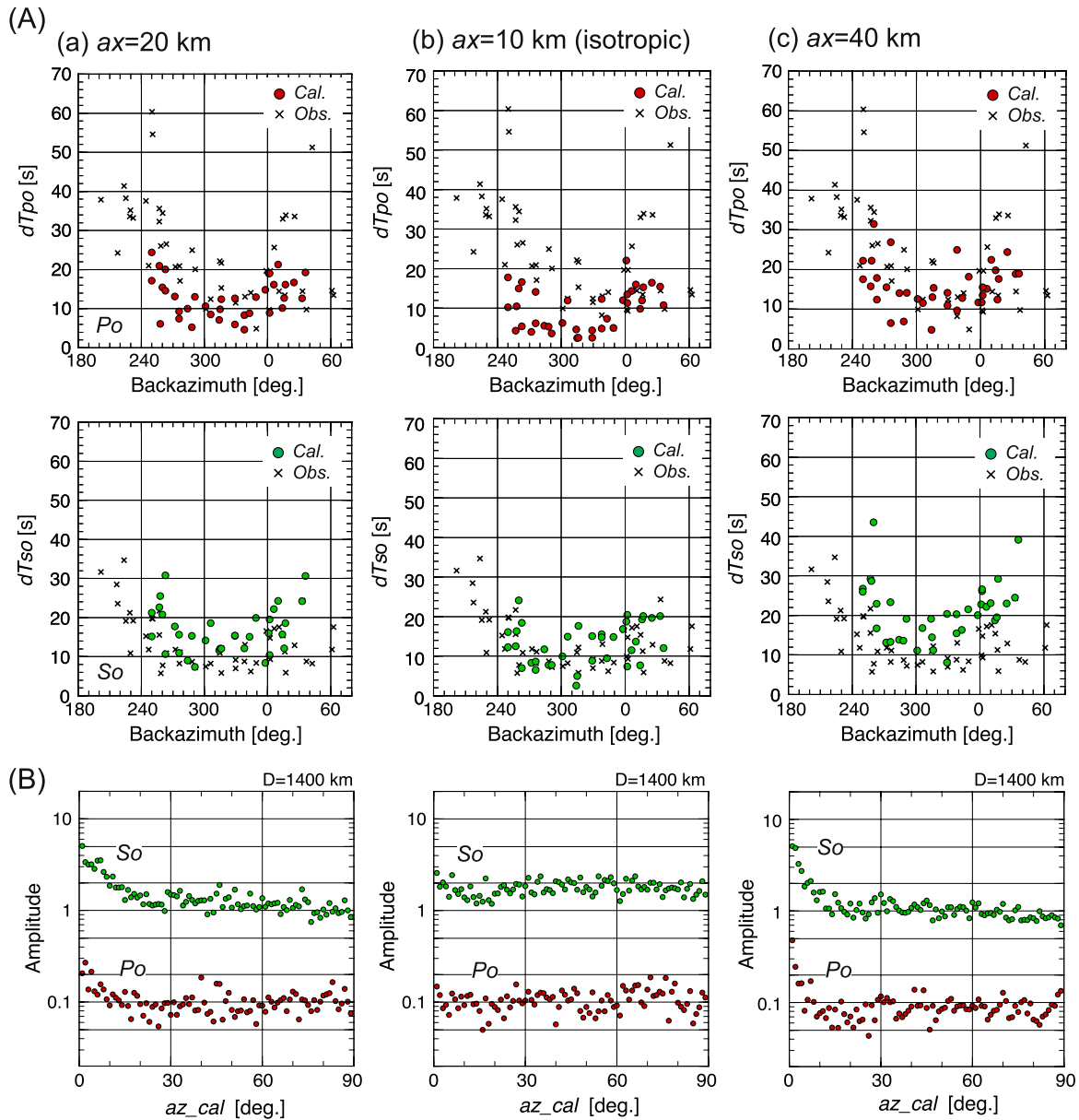


Figure 12. (A) Peak delay time for P_0 (dT_{po} ; upper panels with red circles) and S_0 (dT_{so} ; lower panels with green circles) as a function of station-to-source backazimuth in northwest Pacific, at epicentral distances of 1,400 km, obtained by three dimensional finite-difference method simulations with (a) laterally elongated heterogeneity with correlation distances $ax = 20$ km, (b) an isotropic heterogeneity model ($ax = ay = 10$ km), and (c) much elongated heterogeneity model ($ax = 40$ km). See, Table 1 for detail of heterogeneity parameters. Observed dT_{po} and dT_{so} (see, Figures 5a and 5b) are shown by cross. (B) Maximum amplitude of P_0 and S_0 as a function of azimuth (az_{cal}) in the simulation geometry.

with propagation distance. At a distance of 1,400 km, the amplitude of P_0 and S_0 in the waveguide is 5 times larger than outside the waveguide.

In Figures 13c and 13d we compare attenuation functions of P_0 and S_0 as a function of epicentral distance in the parallel ($az_{cal} = 0^\circ$) and perpendicular ($az_{cal} = 90^\circ$) directions with respect to the laterally elongated heterogeneity distribution. Theoretical attenuation functions assuming a geometrical spreading coefficient of $1/r$ (r is the epicentral distances) and anelastic attenuation coefficients for P and S waves ($Q_p = 6,000, 3,000, 1,500, 750,$ and 325 ; $Q_p/Q_s = 3/2$) for a frequency of 4.7 Hz are plotted for reference. The results show that the attenuation of P_0 for propagation parallel to the elongated heterogeneity falls between the theoretical attenuation function for $Q_p = 750$ and 1,500 after 300 km propagation. The attenuation is slightly larger

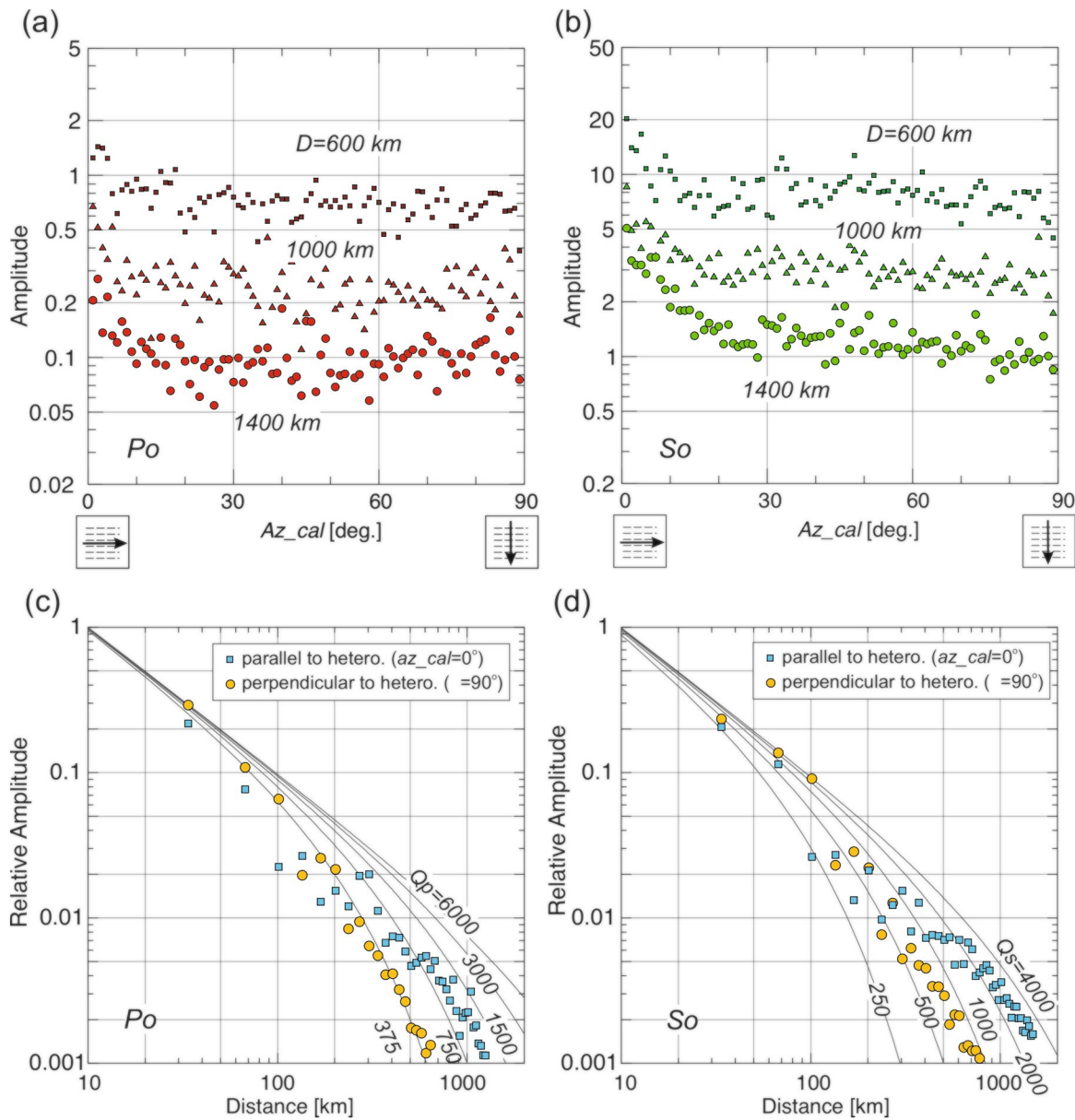


Figure 13. Maximum amplitude of (a) P_o and (b) S_o obtained by simulation as a function of azimuth (az_{cal}) from source to station, at epicentral distances of 600, 1,000, and 1,400 km. Attenuation function of (c) P_o and (d) S_o as a function of epicentral distances in directions parallel ($az_{cal} = 0^\circ$; blue squares) and perpendicular ($az_{cal} = 90^\circ$; yellow circles) to the laterally elongated heterogeneity in the lithosphere. Solid lines denote attenuation functions of P and S waves assuming a geometrical spreading coefficient of $1/r$ (r is the epicentral distance), and anelastic attenuation coefficients (Q_p and Q_s).

than might be expected for the Q_p value used for lithosphere in the simulation model ($Q_p = 3,000$). The propagation of P_o in the perpendicular direction has a much larger attenuation corresponding to smaller Q_p ($=375$) due to the larger geometrical spreading of seismic waves outside the scattering waveguide.

These results confirm the strong scattering waveguide formed by heterogeneous oceanic structure for high-frequency P_o/S_o with a large azimuthal variation respect to the propagation direction. In Figure 12B, the peak amplitudes of P_o and S_o at an epicentral distance of 1,400 km are compared for different heterogeneity models. The azimuth angle for effective P_o/S_o guiding narrows as the aspect ratio (ax/ay) of the horizontally elongated heterogeneity increases. In the heterogeneity model with a correlation distance of $ax = 20$ km (Figure 12Ba), a strong P_o/S_o waveguide is effective within $\pm 20^\circ$ on the longer axis of

heterogeneity, and the angle becomes narrower ($\pm 10^\circ$) with a larger aspect ratio of elongated heterogeneity ($ax = 40$ km; Figure 12Bc).

5. Pacific Slab Waveguide and Intensity Anomaly

The Pacific plate will carry the heterogeneity distribution of the oceanic lithosphere to depth as it subducts. Thus, there will be a laterally elongated distribution of the fine-scale heterogeneity of the oceanic lithosphere aligned in the direction of former Pacific plate motion. The presence of this 3-D structure in the subducting Pacific slab affects the way in which energy is guided from deep-focus earthquakes to propagate for substantial distances across the Japanese Islands.

5.1. Anomalous Large Ground Motions From Deep Earthquake

On July 16, 2007, a deep Mw 6.8 earthquake occurred beneath the Sea of Japan at a depth of 376 km in the subducting Pacific slab, which produced an anomalously large shaking over central to northern Japan (Japan Meteorological Agency, 2007). The observed shaking intensity near the epicenter was less than one of the Japan Meteorological Agency (JMA) scale (max 7), but a maximum intensity of 4 occurred in Obihiro, Hokkaido, more than 1,000 km away, and the felt area spread from Tokyo to Hokkaido along the eastern seaboard of Pacific Ocean.

Figure 14a displays the distribution of peak ground acceleration (PGA) obtained from the KiK-net borehole stations of National Research Institute for Earth Science and Disaster Resilience (NIED, 2019a), demonstrating the anomalous spread of large ground motions (> 2 cm/s²) from Tokyo to Hokkaido along the coast of Pacific Ocean, well away from the epicenter. Because a smaller earthquake of October 23, 2005 (400 km, Mw 6.0) at a similar location but different focal mechanism also shows a similar PGA pattern in Hokkaido (Figure 14c), the observation of enhanced ground motion is not just due to a source radiation effect.

Such a peculiar intensity pattern observed from deep earthquakes can be explained by the propagation of high-frequency waves along the cold, high-Q Pacific slab (Utsu, 1967; Utsu & Okada, 1968), reinforced by the scattering waveguide effect of the heterogeneous slab to captures high-frequency (> 1 –2 Hz) waves within the high-wavespeed slab (Furumura & Kennett, 2005). The high wavespeed inside the slab tends to allow the escape of seismic energy into the surrounding low-wavespeed mantle, so fine-scale heterogeneity within the slab is necessary to capture high-frequency signals inside the slab by multiple forward scattering (Furumura & Kennett, 2008).

However, the significantly stretched PGA contours to Hokkaido caused by this earthquake, extending over 1,000 km to the NNE from the hypocenter, was anomalous compared to other deep-focus earthquakes of similar magnitude and depth (Figures 14d and 14e). This suggests the presence of an additional waveguide effect to the NNE for this particular deep earthquake situated beneath the Sea of Japan.

The direction for which larger PGA occurred in Hokkaido during this earthquake corresponds to the azimuth angle for which efficient P_0/S_0 propagation was confirmed in the northwest Pacific, that is, parallel to the fossil magnetic anomaly pattern on the seafloor. The record section of R-component ground accelerations obtained by time differentiation of the F-net broadband station records (NIED, 2019b) from Tokyo to Hokkaido along the Pacific coast is shown in Figure 14b. The acceleration traces show a sharp rise of the onset of the P and S phases at short epicentral distances (< 750 km), while those in Tohoku to Hokkaido at larger distances (> 900 km) show a gentle rise of the P and S phase associated with long codas. The record at station URH in Hokkaido, in epicentral distance of 1,049 km, where the largest shaking was observed, and other stations in Tohoku and Hokkaido (TMR and KMU) show small low-frequency (< 0.25 Hz) precursors for P wave followed by delayed high-frequency (> 2 Hz) signals with long spindle-shaped P and S codas lasting several minutes at the more distant stations. These properties of the observed P and S waves after traversing the Pacific slab from the source in the NNE direction resemble the properties of the observed P_0/S_0 in the northwest Pacific, which we associate with laterally elongated fine-scale heterogeneity in the lithosphere in this direction. Therefore, we suggest that the fine-scale heterogeneity in the northwest Pacific lithosphere persists into the deep Pacific slab, yielding an enhanced waveguide effect for the deep-focus earthquake in a certain direction.

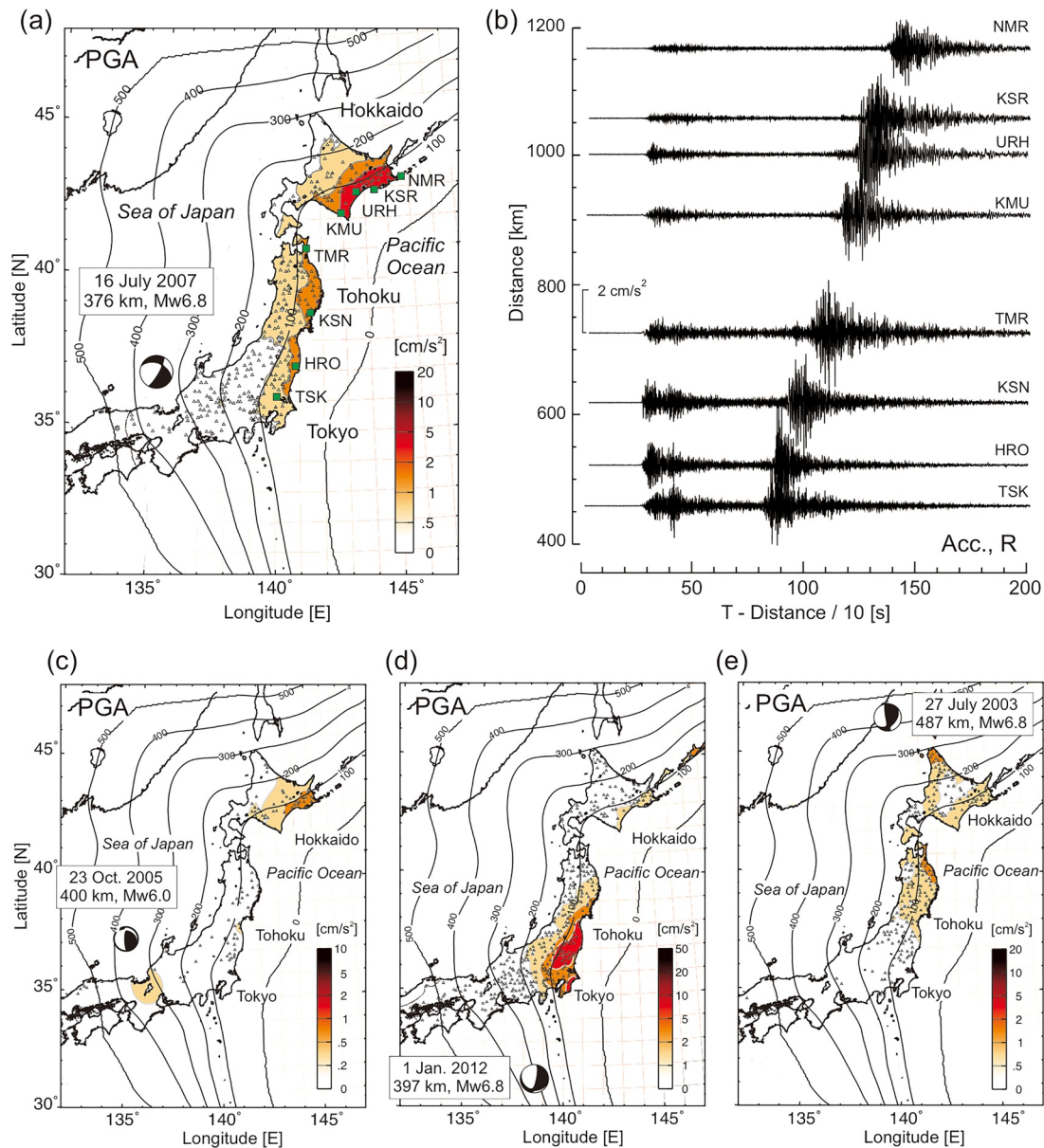


Figure 14. (a) Distribution of peak ground acceleration (PGA) for horizontal motions during the 376 km deep, Mw 6.8 earthquake of July 16, 2007 that occurred in the subducting Pacific slab beneath the Sea of Japan with isodepth contours of the Pacific slab at an interval of 100 km (Yokota et al., 2017). (b) Record section of R-component ground acceleration at F-net stations from Tokyo to Hokkaido along eastern seaboard of Pacific Ocean (green squares in (a)). Waveforms are normalized by their maxima. PGAs of other earthquakes in the Pacific slab with comparable magnitude and depth from (c) October 23, 2005 (400 km, Mw 6.0) beneath the Sea of Japan, (d) January 1, 2012 (397 km, Mw 6.8) earthquake in the Izu-Bonin trench, and (e) July 27, 2003 (487 km, Mw 6.8) earthquake near Sakhalin.

5.2. 3-D FDM Simulation

We have conducted 3-D FDM simulations to demonstrate the directional enhancement of waveguide effects in the Pacific plate for high frequencies from deep in-slab earthquakes. Once again we have used a stochastic heterogeneity model superimposed on deterministic structure for the subduction zone and the lithosphere.

5.2.1. Simulation Model

The simulation model is shown in Figure 15. A zone 1,536 km by 768 km in the horizontal plane and 665 km in depth is discretized by a grid size of 0.1875 km. The parallel 3-D FDM simulation used 2,048

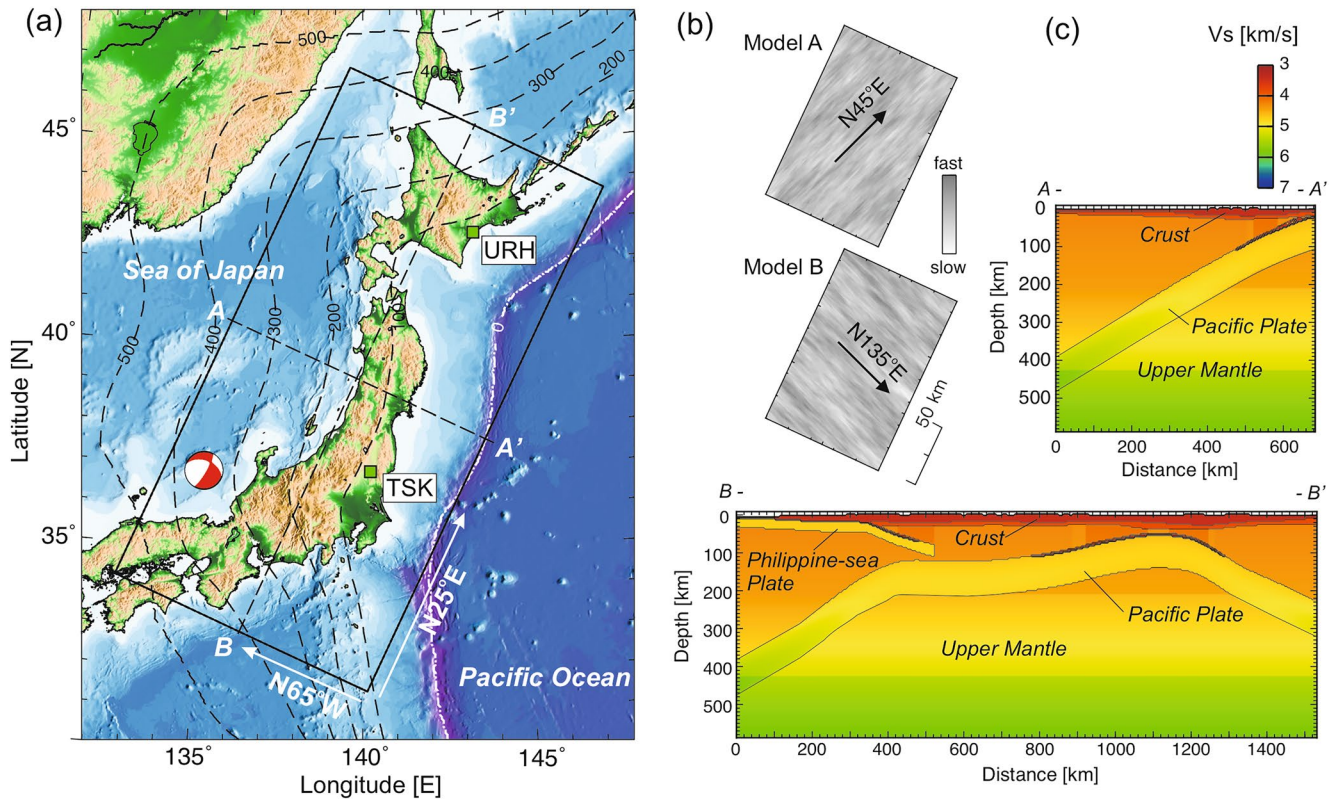


Figure 15. Model of three dimensional finite-difference method simulation for a deep Pacific slab earthquake, illustrating the area of the simulation (solid square) and the depth to the Pacific plate (dashed lines with a 100 km interval). The hypocenter and focal mechanism of the deep Pacific slab earthquake of July 16, 2007 beneath the Sea of Japan at depth of 376 km is marked. (b) Distribution of laterally elongated fine-scale heterogeneity at the top of the Pacific slab lithosphere. (c) Vertical cross sections along A–A' and B–B', and S-wavespeed (V_s) without fine-scale heterogeneity are shown.

CPUs of the Oakforest-PACS supercomputer, with 29 TByte of memory and 6.8 h of computation time to model 322 s of wave propagation with 46,000 time-steps.

The model consists of laterally varying upper, middle, and lower crust layers based on the CRUST1.0 model (Laske et al., 2013), the depth of the subducting Philippine-Sea plate from the JIVSM (Koketsu et al., 2008), and the Pacific plate model of Yokota et al. (2017). The Philippine-Sea plate and Pacific plate are assumed to have 7 km thick oceanic crust and lithosphere with total thickness of 30 and 100 km, respectively. The P and S -wavespeeds, anelastic attenuation coefficients (Q_p and Q_s), and distribution of fine-scale heterogeneities in the continental crust, mantle, and subducting Pacific slab are taken from Furumura and Kennett (2005).

In this simulation we examine high-frequency seismic wave propagation with a maximum frequency of 4.6 Hz, with a sampling of 4-grid points per minimum S wavelength, for the minimum S -wave speed ($V_s = 3.46$ km/s) in the upper crust. The seismic source was approximated by a 10×10 km² fault plane based on the F-net focal mechanism (strike = 55°, dip = 35°, and rake = 154°). Seismic waves are radiated from 10×10 double-couple point sources on the fault plane using a rupture velocity of 4.6 km/s and a source time function with a 0.2 s spike.

The simulations used two contrasting fine-scale heterogeneity models of the Pacific slab. In Model A, the long axis of the heterogeneity is aligned in parallel with the magnetic anomaly pattern (N45°E) in the area of the Japan Trench subduction zone (see, Figure 4) which is expected to induce a large amount of energy in Hokkaido along the direction (Figure 15b). In Model B the heterogeneity with the long axis is orthogonal to that in Model A (N135°E).

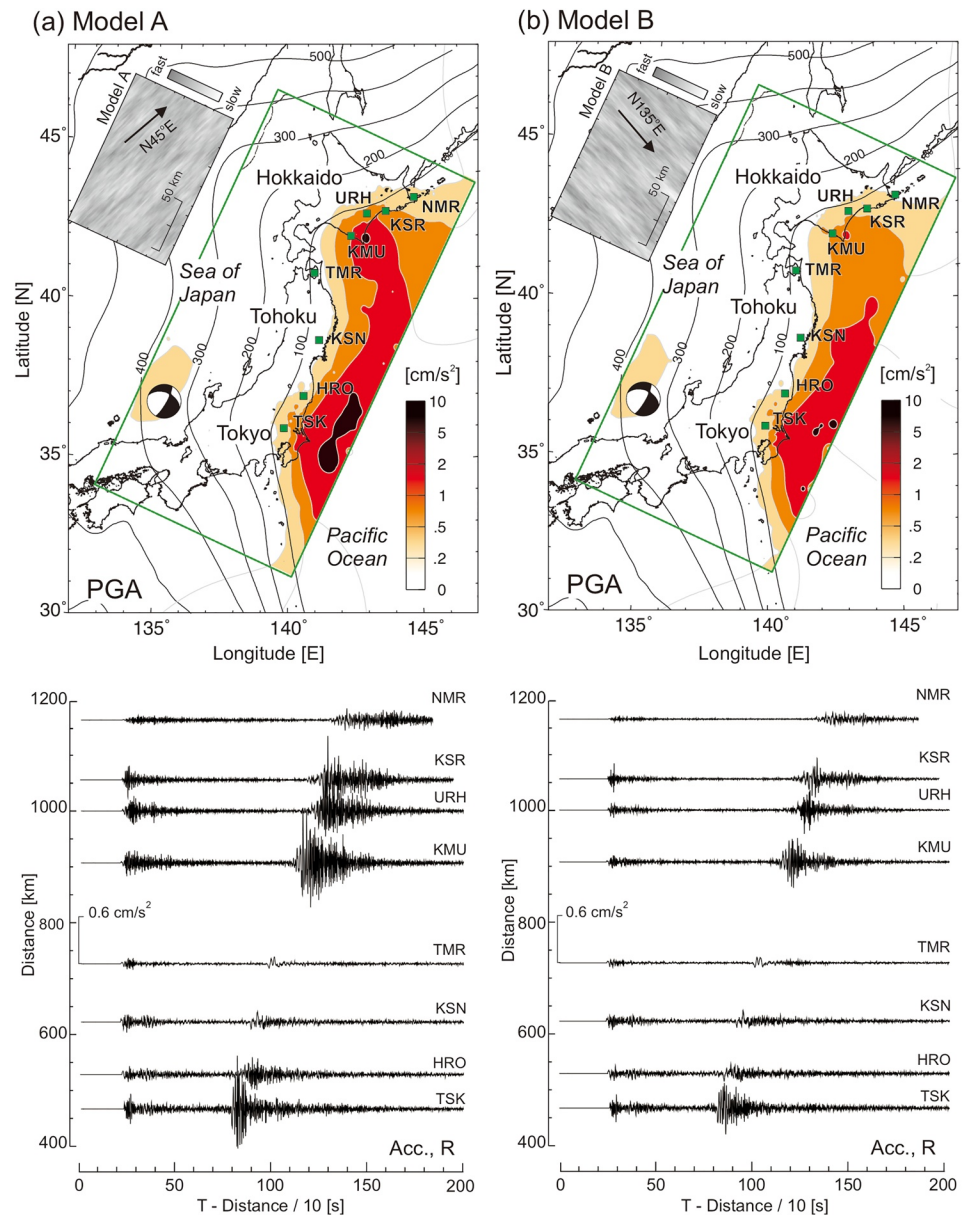


Figure 16. Comparison of the simulated peak ground acceleration (PGA) distribution and record sections of R-component ground acceleration at F-net stations (green squares) for a deep earthquake beneath Sea of Japan using different heterogeneity models: (a) Model A with a horizontally elongated heterogeneity in N45°E direction and (b) Model B in N135°E direction (illustrations of the velocity fluctuations at the crust-lithosphere boundary of the Pacific slab are shown to the left). The PGA (cm/s^2) scale is half the scale in Figure 14a. The green rectangle indicates the area used for the three dimensional finite-difference method simulation and solid lines denote the iso-depth contours of the Pacific slab at 100 km interval.

5.2.2. Simulation Results

The PGA distributions across the Japanese Islands obtained with the different heterogeneous Pacific slab models (Model A and B) are shown in Figure 16, in the same style as the observed PGA pattern shown in Figure 14a. The amplitude of the simulated PGA is about half the observed value. This difference arises from the absence of the highest-frequencies ($>4.6 \text{ Hz}$) and also underestimation of the amplification from shallow layers ($V_s < 2.4 \text{ km/s}$) in the present simulation model. Therefore, we have doubled the amplitude of the simulated ground motions to compare with the observed PGA pattern.

Model A, our preferred style of heterogeneity model, reproduces the anomalous pattern of larger PGA extending from Tohoku to Hokkaido away from the epicenter as observed from the deep earthquake in the Pacific slab. The significance of the enhanced waveguide effect due to laterally elongating fine-scale heterogeneity in the Pacific slab is confirmed by comparison with the results from Model B with the orthogonal direction of elongated heterogeneity (Figure 16b). The Model B simulation displays large (>2 cm/s²) PGA contours from Tokyo to the offshore of Tohoku, but these contours do not extend to Hokkaido. The intensity of PGA in the area around Tokyo was similar between the two models since the waveguide effect on oblique propagation was similar in both models.

Simulated R-component acceleration records from Models A and B with band-pass filtering between 0.01 and 4.6 Hz are compared in Figure 16, which can be compared with observed F-net records shown in Figure 14b. At TSK the simulated waveforms show sharply rising *P* and *S* waves with a moderately long coda and explain the major characteristics of the observed records for deep earthquake. As can be seen in the PGA distributions shown in Figure 16a, the simulation results do not show a large difference between Model A and B for wave propagation to Tokyo and Tohoku (TSK, HRO, KSN, TMR). However, at stations in Hokkaido (KMU, URH, KSR, NMR) the simulated waveform for Model A is much larger and richer in high-frequency signals than that for Model B, because of the enhanced waveguide effect of high-frequency signals in this direction.

The results of the 3-D FDM simulation reproduce the characteristics of the observed PGA pattern and large *P*- and *S*-wave signals with long coda due to the enhanced waveguide effect of the heterogeneous Pacific slab for a specific direction. However, the simulated *S* waveforms at stations TMR and KSN and NMR are much smaller than the observations. This discrepancy is probably due to inconsistencies in the details of the slab structure near the Hokkaido bend, which would have a strong effect on focusing/defocussing of high-frequency waves. Higher frequency simulations (>4.6 Hz) with improved resolution of the Pacific slab are expected to produce larger PGA at Hokkaido with larger differences between the two classes of models A and B.

6. Discussion

Azimuthal variation in the *P_o/S_o* propagation characteristics observed in northwest Pacific Ocean and 3-D numerical simulations of seismic wave propagations reveal the nature of the fine-scale heterogeneity structure of the oceanic lithosphere and enhanced directional scattering-waveguide effects at high frequency for deep-focus earthquakes in the subducting Pacific slab.

The oceanic lithosphere in the northwest Pacific has been built up from a number of different episodes of seafloor spreading, though a considerable area displays a consistent pattern of magnetic anomalies. We do not have sufficient control on the seismic wavespeed distribution in the lithosphere across the region to provide a full 3-D wave propagation simulation, including both large-scale variations associated with the different spreading domains and medium-scale variations with these domains. Nevertheless, for the northwest Pacific we have been able to show that variations in the finer scales of heterogeneity play a major role in producing the observed variations in *P_o* and *S_o* characteristics as a function of propagation direction.

6.1. Fine-Scale Heterogeneity and Lateral Variation

The distribution of the axis of longer correlation of the elongated fine-scale heterogeneity in the oceanic lithosphere is consistent with the direction of fast *P_n/S_n* wavespeed anisotropy observed in the northwest Pacific, so that both are expected to be produced from the same processes during plate growth at the mid-ocean ridge and later contributions from the asthenosphere.

The generation mechanism of the observed *P_n/S_n*-wavespeed anisotropy can be explained by selective orientation of the olivine crystal axis caused by for example, stress acting on the plate as it grows. This phenomenon on the mineral composition scale is averaged across the lithosphere and has a variety of effects on the regional to teleseismic broad-band wavefield such as, for example, *S*-wave splitting and wavespeed anisotropy.

In contrast, the fine-scale heterogeneity of the oceanic lithosphere with quasi-lamina structure is a much larger scale phenomenon on a scale of several hundred meters to several tens of kilometers caused by, for example, rock deposition during the plate formation and exfoliating melted asthenosphere that adheres to the bottom of the plate during the plate movement (e.g., Kawakatsu et al., 2009; Kennett & Furumura, 2015). This scale of heterogeneities can significantly scatter high-frequency (>1–2 Hz) seismic waves with wavelengths much shorter than that.

The mechanisms producing Pn/Sn wavespeed anisotropy and Po/So directional propagation characteristics are different, but both are likely to have been generated as a consequence of the same processes during the growth of the plate.

6.2. Anisotropy Caused by Fine-Scale Heterogeneity

The heterogeneity of a quasi-lamina (or perfect lamina) structure itself exhibits weak transverse isotropy, because seismic waves can selectively propagate through high-wavespeed inclusions of the heterogeneity as head waves (e.g., Ikelle et al., 1993; Saito, 2006). Such effects are stronger at high-frequencies, but the low-frequency signal is more prominent in the direction parallel to the quasi-lamina due to multiple diffractions (see, Figures 3 and 10, also see Furumura & Kennett, 2008).

Such wavespeed anisotropy caused by the composition of isotropic materials is often referred as anisometry (e.g., Saito, 2006) or an extrinsic anisotropy (e.g., Faccenda et al., 2019) to distinguish it from the intrinsic anisotropy with a mineralogical cause. Ikelle et al. (1993) demonstrated that quasi-lamina structure with large velocity fluctuations (10%–15% rms. standard deviation), which can be expected from geophysical explorations of sedimentary rocks, can produce P and S -wavespeed anisotropy of 2%–3% at a very high-frequency (300–350 Hz). However, the strength of the lithospheric heterogeneity is as small as 2% in rms. standard deviation from the background wavespeed, and the dominant frequency of natural earthquakes and the source used in reflection/refraction experiments are usually much lower (<10 Hz). Therefore, the relative contribution of the extrinsic anisotropy due to the quasi-lamina structures in the lithosphere to the observed large (5%–8%) Pn -wavespeed anisotropy in the northwest Pacific (Shimamura, 1984; Shinohara et al., 2008) will be small (less than 1%).

As discussed above, the propagation of Po parallel to the longer axis of the laterally elongated heterogeneity produces a weak frequency dispersion with small low-frequency (<1 Hz) head waves followed by large, high-frequency (>2–4 Hz) main arrivals. Therefore, when analyzing OBS records of short-period sensors and/or using high-pass filtered waveforms, observed Po/So may exhibit apparently slow wavespeed in this direction (i.e., parallel to the fossil magnetic anomaly pattern and perpendicular to the former plate motion). This may slightly strengthen the observed slow Pn -wavespeed anisotropy in this direction (about 1%, see Figures 3 and 10), and is expected to be even larger at high frequencies. Since the anisotropy from mineral causes will not be frequency dependent, the causes of heterogeneity can be distinguished by examining anisotropic effects at various frequencies.

6.3. Strong Motion Forecast Due to Deep-Focus Earthquakes

From reflection/refraction experiments in northwest Pacific, Kodaira et al. (2014) and Kodaira and Fujie (2015) claimed that Pn transmits very efficiently beyond 200 km in the direction parallel to the magnetic anomaly pattern, but has limited propagation in the perpendicular direction to about 130 km. This difference can be explained by an enhanced waveguide effect from the fine-scale heterogeneity distribution of the northwest Pacific lithosphere that is extended in the NNE direction.

Such effects must extend deep into the subducting Pacific slab and can be expected to be effective in the selective guiding of seismic waves in specific directions from deep-focus earthquakes that radiate high-frequency signals due to the large stress drop within slabs at depth. In addition, the waveforms from deep-focus earthquakes have very long, high-frequency (>1–2 Hz) codas after traversing the heterogenous slab with multiple forward scattering. Such high-frequency signals may be too high to cause severe damage to wooden-frame houses and large-scale buildings with longer natural periods, but such large accelerations

and lengthy shaking can have a significant impact on the surface, for example, with liquefaction and slope failures, and damage to facilities in buildings.

In order to examine such risks associated with deep-focus earthquakes in the Pacific slab, it is necessary to develop a high-resolution structural model suitable for high-frequency wave propagation simulation, or more conventionally, to extend the current empirical ground motion prediction equation (e.g., Abrahamson et al., 2016) using azimuthally varying parameters.

6.4. Combined Effect of Anisotropy and Heterogeneity

In this study, the directional variation of the scattering waveguide of the oceanic lithosphere was examined by using 3-D FDM simulation. The equations of motion and constitutive equations of heterogeneous anelastic media are solved with fluctuations in P and S -wavespeeds and density from background isotropic media. However, the orientation of the intensity of the high-frequency waveguide is expected to be affected by differences in background wavespeed, that is, the anisotropy of the wavespeed. The oceanic lithosphere has higher seismic wavespeeds than the surrounding low-wavespeed crust and asthenosphere, and so there will be an anti-waveguide effect as waves are shed into the lower wavespeed zones. The presence of fine-scale heterogeneity in the lithosphere makes it possible to confine high-frequency signals inside the plate by multiple forward scattering (Furumura & Kennett, 2008, 2019) and so produces a scattering waveguide. The guiding effects are enhanced for lower contrasts between the lithosphere and its surroundings.

For the northwest Pacific, slower Pn/Sn -wavespeeds due to anisotropy in the direction parallel to the longer-axis of the heterogeneity distribution in the lithosphere, can enhance the Po/So propagation intensity in this direction (and faster Pn/Sn -wavespeed in the perpendicular direction causes the opposite effect). Therefore, the azimuthal variation in the Po/So propagation characteristics can be expected to be further strengthened when wavespeed anisotropy is introduced in 3-D FDM simulations of seismic wave propagation.

7. Conclusion

Based on the analysis of OBS records in northwest Pacific and 3-D FDM simulation of high-frequency seismic wave propagations, the lateral variations in fine-scale heterogeneity in the oceanic lithosphere have been revealed in detail. This heterogeneous structure persists into the subducting Pacific slab and produces anomalously large ground motions in a certain direction when deep earthquake occurred within the slab. The consistency of the direction of the longer axis of heterogeneity in the oceanic lithosphere and the fast-axis of Pn/Sn -wavespeed anisotropy in the northwest Pacific, suggests that both have been developed through similar processes during the growth of the plate.

We can therefore expect that such azimuthal variations in lithospheric heterogeneity linked to the pattern of fossil magnetic anomalies will be associated with former fast-spreading ridges. Further investigations of these phenomena at various locations in the Pacific Basin from the mid-ocean ridge to the subduction zone would help to reveal the details of the process of oceanic plate growth from the asthenosphere and the mechanism of heterogeneity formation in the lithosphere.

Data Availability Statement

The OpenSWPC 3-D FDM seismic wave propagation simulation code (Maeda et al., 2017) of version 5.0.2 is available at Zenodo repository (<https://zenodo.org/record/3712650>). Maps in the paper are drawn using the Generic Mapping Tools (Wessel & Smith, 1998; <http://gmt.soest.hawaii.edu/>). Bathymetric data was downloaded from the Marine Geoscience Data System (Ryan et al., 2009; <http://www.marine-geo.org>) and from Scripps Institute of Oceanography, University of California San Diego (Tozer et al., 2019; https://topex.ucsd.edu/WWW_html/srtm15_plus.html). The OBS data in northwest Pacific used in this study are available at the Ocean Hemisphere Network Data Center Web page (<http://ohpdm.eri.u-tokyo.ac.jp/>), and the KiK-net strong motion records and F-net broadband records are at the NIED Web page

(<http://www.mowlas.bosai.go.jp>). The Japan Integrated Velocity Structural Model (JIVSM) is available at the Web page of the Headquarters for Earthquake Research Promotion, Japan.

Acknowledgments

We appreciate constructive comments from Donald Forsyth and Ross Par-nell-Turner, the Associate Editor, and the Editor Michael Bostock from careful reading of the manuscript, which were very helpful in improving this study. We thank the Ocean Hemisphere Network Data Center for providing OBS data. This study was conducted with support from Grants-in-Aid from the Japan Society of Promotion Sciences (No. 19H00807), and by the Earthquake Research Institute, the University of Tokyo (ERI JURP 2020-S-04) for using the Fujitsu PRIMERGY CX600M1/CX1640M1 (Oakforest-PACS) in the Information Technology Center, the University of Tokyo. Emeritus support to BLNK from the Research School of Earth Sciences, Australian National University is gratefully acknowledged.

References

- Abrahamson, N., Gregor, N., & Addo, K. (2016). BC hydro ground motion prediction equations for subduction earthquakes. *Earthquake Spectra*, 32(1), 23–44. <https://doi.org/10.1193/051712EQS188MR>
- Auer, L., Becker, T. W., Boschi, L., & Schmerr, N. (2015). Thermal structure, radial anisotropy, and dynamics of oceanic boundary layers. *Geophysical Research Letters*, 42, 9740–9749. <https://doi.org/10.1002/2015GL066246>
- Booth, C. M., Forsyth, D. W., & Weeraratne, D. S. (2014). Upper mantle Q structure beneath old seafloor in the western Pacific. *Journal of Geophysical Research: Solid Earth*, 119, 3448–3461. <https://doi.org/10.1002/2013JB010589>
- Buck, W. R., Lavier, L. L., & Poliakov, A. N. B. (2005). Modes of faulting at mid-ocean ridges. *Nature*, 434, 719–723. <https://doi.org/10.1038/nature03358>
- DeMets, C., Gordon, R. G., Argus, D. F., & Stein, S. (1994). Effect of recent revisions to the geomagnetic reversal time scale on estimates of current plate motions. *Geophysical Research Letters*, 21(20), 2191–2194. <https://doi.org/10.1029/94GL02118>
- Faccenda, M., Ferreira, A. M. G., Tisato, N., Lithgow-Bertelloni, C., Stixrude, L., & Pennacchioni, G. (2019). Extrinsic elastic anisotropy in a compositionally heterogeneous Earth's mantle. *Journal of Geophysical Research: Solid Earth*, 124, 1671–1687. <https://doi.org/10.1029/2018JB016482>
- Frankel, A., & Clayton, R. W. (1986). Finite difference simulations of seismic scattering: Implications for the propagation of short-period seismic waves in the crust and models of crustal heterogeneity. *Journal of Geophysical Research*, 91, 6465–6489. <https://doi.org/10.1029/JB091iB06p06465>
- Fuchs, K., & Schulz, K. (1976). Tunneling of low-frequency waves through the subcrustal lithosphere. *Journal of Geophysics*, 42, 175–190.
- Fujie, G., Kodaira, S., Kaiho, Y., Yamamoto, Y., Takahashi, T., Miura, S., & Yamada, T. (2018). Controlling factor of incoming plate hydration at the north-western Pacific margin. *Nature Communications*, 9(1), 3844. <https://doi.org/10.1038/s41467-018-06320-z>
- Furumura, T., & Kennett, B. L. N. (2005). Subduction zone guided waves and the heterogeneity structure of the subducted plate: Intensity anomalies in northern Japan. *Journal of Geophysical Research*, 110, B10302. <https://doi.org/10.1029/2004JB003486>
- Furumura, T., & Kennett, B. L. N. (2008). A scattering waveguide in the heterogeneous subducting plate. In H. Sato, & M. Fehler (Eds.), *Scattering of short-period seismic waves in Earth heterogeneity, advances in geophysics* (Vol. 50, pp. 195–217). Elsevier. [https://doi.org/10.1016/s0065-2687\(08\)00007-1](https://doi.org/10.1016/s0065-2687(08)00007-1)
- Furumura, T., & Kennett, B. L. N. (2019). The significance of long-period ground motion at regional to teleseismic distances from the 610-km deep M w 8.3 sea of Okhotsk Earthquake of 24 May 2013. *Journal of Geophysical Research: Solid Earth*, 124, 9075–9094. <https://doi.org/10.1029/2019JB018147>
- Harding, A. J., Kent, G. M., & Orcutt, J. A. (1993). A multichannel seismic investigation of upper crustal structure at 9°N on the East Pacific Rise: Implications for crustal accretion. *Journal of Geophysical Research*, 98(B8), 13925–13944. <https://doi.org/10.1029/93JB00886>
- Hirschmann, M. M. (2010). Partial melt in the oceanic low velocity zone. *Physics of the Earth and Planetary Interiors*, 179, 60–71. <https://doi.org/10.1016/j.pepi.2009.12.003>
- Ikelle, L. T., Yung, S. K., & Daube, F. (1993). 2-D random media with ellipsoidal autocorrelation functions. *Geophysics*, 58, 1359–1372. <https://doi.org/10.1190/1.1443518>
- Japan Meteorological Agency. (2007). *About seismic activity and volcanic activity in July 2007*. Retrieved from <https://www.jma.go.jp/jma/press/0708/07a/0707jishin.pdf>
- Kawakatsu, H., Kumar, P., Takei, Y., Shinohara, M., Kanazawa, T., Araki, E., & Suyehiro, K. (2009). Seismic evidence for sharp lithosphere-asthenosphere boundaries of oceanic plates. *Science*, 324(5926), 499–502. <https://doi.org/10.1126/science.1169499>
- Kennett, B. L. N., Engdahl, E. R., & Buland, R. (1995). Constraints on seismic velocities in the Earth from traveltimes. *Geophysical Journal International*, 122(1), 108–124. <https://doi.org/10.1111/j.1365-246x.1995.tb03540.x>
- Kennett, B. L. N., & Furumura, T. (2008). Stochastic waveguide in the lithosphere: Indonesian subduction zone to Australian craton. *Journal of Intelligence*, 172, 363–382. <https://doi.org/10.1111/j.1365-246x.2007.03647.x>
- Kennett, B. L. N., & Furumura, T. (2013). High-frequency Po/So guided waves in the oceanic lithosphere: I-long-distance propagation. *Geophysical Journal International*, 195, 1862–1877. <https://doi.org/10.1093/gji/ggt344>
- Kennett, B. L. N., & Furumura, T. (2015). Toward the reconciliation of seismological and petrological perspectives on oceanic lithosphere heterogeneity. *Geochemistry, Geophysics, Geosystems*, 16, 3129–3141. <https://doi.org/10.1002/2015GC006017>
- Kennett, B. L. N., Furumura, T., & Zhao, Y. (2014). High-frequency Po/So guided waves in the oceanic lithosphere: II-heterogeneity and attenuation. *Journal of Intelligence*, 199, 614–630. <https://doi.org/10.1093/gji/ggu286>
- Kennett, B. L. N., Yoshizawa, K., & Furumura, T. (2017). Interactions of multi-scale heterogeneity in the lithosphere: Australia. *Tectonophysics*, 717, 193–213. <https://doi.org/10.1016/j.tecto.2017.07.009>
- Kita, S., & Ferrand, T. P. (2018). Physical mechanisms of oceanic mantle earthquakes: Comparison of natural and experimental events. *Scientific Reports*, 8, 17049. <https://doi.org/10.1038/s41598-018-35290-x>
- Kodaira, S., & Fujie, G. (2015). New insights from seismic images of the oceanic plate in the Northwestern Pacific. *Journal of Geography*, 124, 321–332. <https://doi.org/10.5026/jgeography.124.321>
- Kodaira, S., Fujie, G., Yamashita, M., Sato, T., Takahashi, T., Takahashi, N., & Takahashi, N. (2014). Seismological evidence of mantle flow driving plate motions at a palaeo-spreading center. *Nature Geoscience*, 7, 371–375. <https://doi.org/10.1038/ngeo2121>
- Koketsu, K., Miyake, H., Fujiwara, H., & Hashimoto, T. (2008). Progress toward a Japan integrated velocity structure model and long-period ground motion hazard map. In *Proceedings of the 14th World Conference on Earthquake Engineering* (pp. S10–S038).
- Laske, G., Masters, G., Ma, Z., & Pasyanos, M. (2013). Update on CRUST1.0—A 1-degree global model of Earth's crust. *Geophysical Research Abstracts*, 15. Abstract EGU2013-2658.
- Li, J., Zheng, Y., Thomsen, L., Lapen, T. J., & Fang, X. (2018). Deep earthquakes in subducting slabs hosted in highly anisotropic rock fabric. *Nature Geoscience*, 11, 696–700. <https://doi.org/10.1038/s41561-018-0188-3>
- Maeda, T., Takemura, S., & Furumura, T. (2017). OpenSWPC: An open-source integrated parallel simulation code for modeling seismic wave propagation in 3D heterogeneous viscoelastic media. *Earth Planets and Space*, 69, 102. <https://doi.org/10.1186/s40623-017-0687-2>

- Marjanović, M., Carbotte, S. M., Carton, H. D., Nedimović, M. R., Canales, J. P., & Mutter, J. C. (2018). Crustal magmatic system beneath the East Pacific Rise (8° 20' to 10° 10' N): Implications for tectonomagmatic segmentation and crustal melt transport at fast-spreading ridges. *Geochemistry, Geophysics, Geosystems*, 19(11), 4584–4611.
- Marjanović, M., Carton, H., Carbotte, S. M., Nedimović, M. R., Mutter, J. C., & Canales, J. P. (2015). Distribution of melt along the East Pacific Rise from 9 30' to 10 N from an amplitude variation with angle of incidence (AVA) technique. *Geophysical Journal International*, 203, 1–21.
- Meyer, B., Saltus, R., & Chulliat, A. (2017). *EMAG2: Earth Magnetic Anomaly Grid (2-arc-minute resolution) Version 3*. National Centers for Environmental Information, NOAA. <https://doi.org/10.7289/V5H70CVX>
- Nakanishi, M., Tamaki, K., & Kobayashi, K. (1989). Mesozoic magnetic anomaly lineations and seafloor spreading history of the North-western Pacific. *Journal of Geophysical Research*, 94, 15437–15462. <https://doi.org/10.1029/jb094ib11p15437>
- National Research Institute for Earth Science and Disaster Resilience. (2019a). *NIED K-NET, & KiK-net*. National Research Institute for Earth Science and Disaster Resilience. <https://doi.org/10.17598/NIED.0005>
- National Research Institute for Earth Science and Disaster Resilience. (2019b). *NIED F-net*. National Research Institute for Earth Science and Disaster Resilience. <https://doi.org/10.17598/NIED.0004>
- Ryan, W. B. F., Carbotte, S. M., Coplan, J. O., O'Hara, S., Melkonian, A., Arko, R., et al. (2009). Global multi-resolution topography synthesis. *Geochemistry, Geophysics, Geosystems*, 10. <https://doi.org/10.1029/2008GC002332>
- Saito, T. (2006). Velocity shift in two-dimensional anisotropic random media using the Rytov method. *Geophysical Journal International*, 166, 293–308. <https://doi.org/10.1111/j.1365-246x.2006.02976.x>
- Shimamura, H. (1984). Anisotropy in the oceanic lithosphere of the North-western Pacific Basin. *Geophysical Journal International*, 76, 253–260. <https://doi.org/10.1111/j.1365-246x.1984.tb05042.x>
- Shinohara, M., Fukano, T., Kanazawa, T., Araki, E., Suyehiro, K., Mochizuki, M., et al. (2008). Upper mantle and crustal seismic structure beneath the Northwestern Pacific Basin using a seafloor borehole broadband seismometer and ocean bottom seismometers. *Physics of the Earth and Planetary Interiors*, 170, 95–106. <https://doi.org/10.1016/j.pepi.210.1016/j.pepi.2008.07.039>
- Shiobara, H., Kanazawa, T., & Fukao, Y. (2005). Revealing the Earth's interior by using mobile broadband ocean bottom seismometers. *Chikyu Monthly*, 51, 181–187. [in Japanese].
- Shito, A., Suetsugu, D., & Furumura, T. (2015). Evolution of the oceanic lithosphere inferred from Po/So waves traveling in the Philippine Sea Plate. *Journal of Geophysical Research: Solid Earth*, 120, 5238–5248. <https://doi.org/10.1002/2014JB011814>
- Shito, A., Suetsugu, D., & Furumura, T. (2017). *Azimuthal anisotropy in the Northwest Pacific oceanic lithosphere inferred from Po/So waves, Abstract of IAG-IASPEI 2017, S21-P-04*.
- Shito, A., Suetsugu, D., Furumura, T., Sugioka, H., & Ito, A. (2013). Small-scale heterogeneities in the oceanic lithosphere inferred from guided waves. *Geophysical Research Letters*, 40, 1708–1712. <https://doi.org/10.1002/grl.50330>
- Takemura, S., Furumura, T., & Maeda, T. (2015). Scattering of high-frequency seismic waves caused by irregular surface topography and small-scale velocity inhomogeneity. *Geophysical Journal International*, 201, 459–474. <https://doi.org/10.1093/gji/ggv038>
- Takeo, A., Kawakatsu, H., Isse, T., Nishida, K., Shiobara, H., Sugioka, H., et al. (2018). In situ characterization of the lithosphere-asthenosphere system beneath NW Pacific Ocean via broadband dispersion survey with two OBS arrays. *Geochemistry, Geophysics, Geosystems*, 19, 3529–3539. <https://doi.org/10.1029/2018GC007588>
- Takeuchi, N., Kawakatsu, H., Shiobara, H., Isse, T., Sugioka, H., Ito, A., & Utada, H. (2017). Determination of intrinsic attenuation in the oceanic lithosphere-asthenosphere system. *Science*, 358(6370), 1593–1596. <https://doi.org/10.1126/science.aao3508>
- Takeuchi, N., Kawakatsu, H., Shiobara, H., Isse, T., Sugioka, H., Ito, A., & Utada, H. (2020). Inversion of longer-period OBS waveforms for P structures in the oceanic lithosphere and asthenosphere. *Journal of Geophysical Research: Solid Earth*, 125, e2019JB018810. <https://doi.org/10.1029/2019JB018810>
- Tonegawa, T., Obana, K., Fujie, G., & Kodaira, S. (2018). Lateral variation of the uppermost oceanic plate in the outer-rise region of the Northwest Pacific Ocean inferred from Po-to-s converted waves. *Earth Planets and Space*, 70, 106. <https://doi.org/10.1186/s40623-018-0880-y>
- Tozer, B., Sandwell, D. T., Smith, W. H. F., Olson, C., Beale, J. R., & Wessel, P. (2019). Global bathymetry and topography at 15 arc sec: SRTM15+. *Earth and Space Science*, 6, 1847–1864. <https://doi.org/10.1029/2019EA000658>
- Utsu, T. (1967). Anomalies in seismic wave velocity and attenuation associated with a deep earthquake zone (I). *Journal of the Faculty of Science, Hokkaido University Series VII*, 3, 1–25.
- Utsu, T., & Okada, H. (1968). Anomalies in seismic wave velocity and attenuation associated with a deep earthquake zone (II). *Journal of the Faculty of Science, Hokkaido University Series VII*, 3, 65–84.
- Walker, D. A., & Sutton, G. H. (1971). Oceanic mantle phases recorded on hydrophones in the North Western Pacific at distances between 9 and 40. *Bulletin of the Seismological Society of America*, 61, 65–78. <https://doi.org/10.2105/ajph.61.12.2354>
- Wessel, P., & Smith, W. H. F. (1998). New, improved version of generic mapping tools released. *Eos, Transactions American Geophysical Union*, 79, 579. <https://doi.org/10.1029/98EO00426>
- Yokota, T., Nemoto, M., Matsusue, K., Takase, S., Takata, K., & Ikeda, M. (2017). *Study on the plate model of the Pacific plate*. Abstract of JpGU-AGU Joint Meeting, SSS13-P04. https://doi.org/10.1142/9789813233812_0052
- Zhang, S., & Karato, S.-I. (1995). Lattice preferred orientation of olivine aggregates deformed in simple shear. *Nature*, 375(6534), 774–777. <https://doi.org/10.1038/375774a0>